ABSTRACT

Title of dissertation: AN INTEGRATED PHOTONIC PLATFORM FOR
QUANTUM INFORMATION PROCESSING

Subhojit Dutta
Doctor of Philosophy, 2021

Dissertation directed by: Professor Edo Waks
Department of Electrical and Computer Engineering

Quantum photonics provides a powerful toolbox with vast applications ranging from quantum simulation, photonic information processing, all optical universal quantum computation, secure quantum internet as well as quantum enhanced sensing. Many of these applications require the integration of several complex optical elements and material systems which pose a challenge to scalability. It is essential to integrate linear and non-linear photonics on a chip to tackle this issue leading to more compact, high bandwidth devices. In this thesis we demonstrate a pathway to achieving several components in the quantum photonic toolbox on the same integrated photonic platform. We focus particularly on two of the more nontrivial components, a single photon source and an integrated quantum light-matter interface. We address the problem of a scalable, chip integrated, fast single photon source, by using atomically thin layers of 2D materials interfaced with plasmonic waveguides. We further embark on the challenge of creating a new material system by integrating rare earth ions with the emerging commercial platform of thin film lithium niobate on insulator. Rare earth ions have found widespread use in classical and quantum information processing. However, these are traditionally doped in bulk crystals which hinder their scalability. We demonstrate an integrated photonic interface for rare earth ions in thin film lithium niobate that preserves the

optical and coherence properties of the ions. This combination of rare earth ions with the chip-scale active interface of thin film lithium niobate opens a plethora of opportunities for compact optoelectronic devices. As an immediate application we demonstrate an integrated optical quantum memory with a rare earth atomic ensemble in the thin film. The new light matter interface in thin film lithium niobate acts as a key enabler in an already rich optical platform representing a significant advancement in the field of integrated quantum photonics.

AN INTEGRATED PHOTONIC PLATFORM FOR QUANTUM INFORMATION PROCESSING

by

Subhojit Dutta

Dissertation submitted to the Faculty of the Graduate School of the
University of Maryland, College Park in partial fulfillment of the
requirements for the degree of
Doctor of Philosophy
2021

Advisory Committee:
Professor Edo Waks, Chair
Professor Kevin Daniels
Professor Thomas Murphy
Professor Cheng Gong
Professor Rajarshi Roy
Professor Robert Newcomb

Dedication

Dedicated to my loved ones

Acknowledgments

I owe my gratitude to all the people who have made this thesis possible andwho have made my graduate experience one that I will cherish forever.

First and foremost, I would like to thank my advisor, Professor Edo Waks, for giving me an invaluable opportunity to work on challenging and extremely interesting projects over the past five years. He has always made himself available for help and advice, and there has never been an occasion when I have knocked on his door and he has not given me time. It has been a pleasure to work with and learn from such an extraordinary individual.

I would also like to thank Professor Kevin Daniels, Professor Cheng Gong, Professor Thomas Murphy, Professor Robert Newcomb and Professor Rajarshi Roy for agreeing to serve on my thesis committee and for sparing their invaluable time reviewing the manuscript.

My colleagues at the Quantum Nanophotonics Group have enriched my graduate life in many ways and deserve a special mention. I would like to thank Dr. Tao Cai for being an excellent mentor in my first two years as a PhD student. I have learned so many experimental techniques by shadowing him in the lab and discussing with him. I would like to thank Dr. Sabyasachi Barik for being a pillar of constant support both inside and outside the lab. I am especially indebted to Prof Elizabeth Goldschmidt for her invaluable contribution and astute guidance in setting up a new research direction in the lab. Her expert advice served as a critical key in enabling the new platform of rare earth doped thin film lithium niobate. My interactions with Dr. ShahriarAghaeimeibodi, Aziz Karasahin, Zhouchen Luo, Mustaf Atabey Buyukkaya, Uday Saha, Yuqi Zhao, Sam Harper, Dr. Robert Pettit, Dr. Jehyung Kim, Dr Zhili Yang, Dr. Youngmin Kim, Dr. Changmin Lee, Dr. Changmu Han, Yu Shi, Dr Dima Farfurnik, Xinyuan Zheng and Harjot Singh have always been very fruitful.

I am grateful for the support from the staff in the UMD Nanofabrication Center: Tom

Loughran, Mark Lecates, Jon Hummel, John Abrahams and Wen-an Chiou. I would also like to thank all the staff members in IREAP, past and present, Bryan Quinn, Don Schmadel, Thomas Weimar, Jennifer Morales, Leslie Delabar, Nancy Boone, Taylor Prendergast, Dorothea Brosius Nolan Ballew, Don Schmadel and Judi Cohn Gorski.

I cannot express in words how fortunate I am to have parents who have raised me to be independent, resilient, honest and passionate in all my pursuits. Special thanks to my sister and little brother whose enthusiasm and belief in me continue to power me through every day. Lastly, I am incredibly lucky to have Suranjana in my life. Her continued support at every step has shaped my journey and made it possible.

I would like to thank Sabyasachi, Swarnav, Soubhik, Sarthak, Harjot and Tamoghna whose camaraderie has made College Park a home away from home.

I would like to acknowledge financial support from the Office of Naval Research (ONR), Air Force Office of Scientific Research (AFOSR), Sloan Foundation and the Physics Frontier Center (PFC) at the Joint Quantum Institute (JQI) for all the projects discussed herein.

It is impossible to remember all, and I apologize to those whom I have inadvertently left out.

Lastly, thank you all!

Table of Contents

Chapter 1: Introduction

Chapter 2: A Fast Integrated Single Photon Source

Chapter 3: An Integrated Photonic Platform For Rare Earth Ions In Thin Film Lithium Niobate

Chapter 4: A Quantum Memory In Thin Film Lithium Niobate

Chapter 5: Conclusion and Outlook

Appendix 1: A Fast Integrated Single Photon Source

Appendix 2: Rare Earth Doped Thin Film Lithium Niobate

List of Figures

Chapter 1: Introduction

Quantum photonics provides a powerful toolbox with a plethora of applications ranging from all-optical quantum computation, long distance quantum networks, quantum simulation as well as quantum sensing.

1.1 Linear Optical Quantum Computing

Linear Optical Quantum Computing is a paradigm of quantum computation, allowing universal quantum computation. This uses photons as information carriers, mainly uses linear optical elements, or optical instruments (including reciprocal mirrors and waveplates) to process quantum information and uses photon detectors and quantum memories to detect and store quantum information.

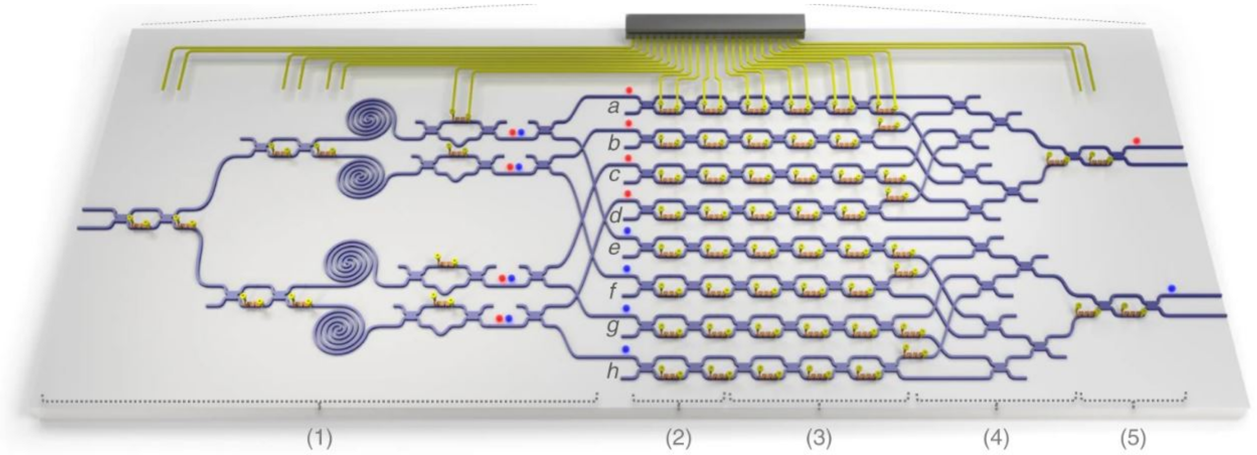

Figure 1.1 Large-scale silicon quantum photonic chip implementing arbitrary two-qubit processing.[1]

The device above is the first universal two qubit quantum processor[1] with over 200 optical elements integrated on chip. It includes five functional parts, which carry out the following: (1) generating ququart entanglement; (2) preparing initial single-qubit states; (3) implementing single-qubit operations; (4) realizing linear combination; (5) changing the measurement basis.

1.2 The Quantum Internet

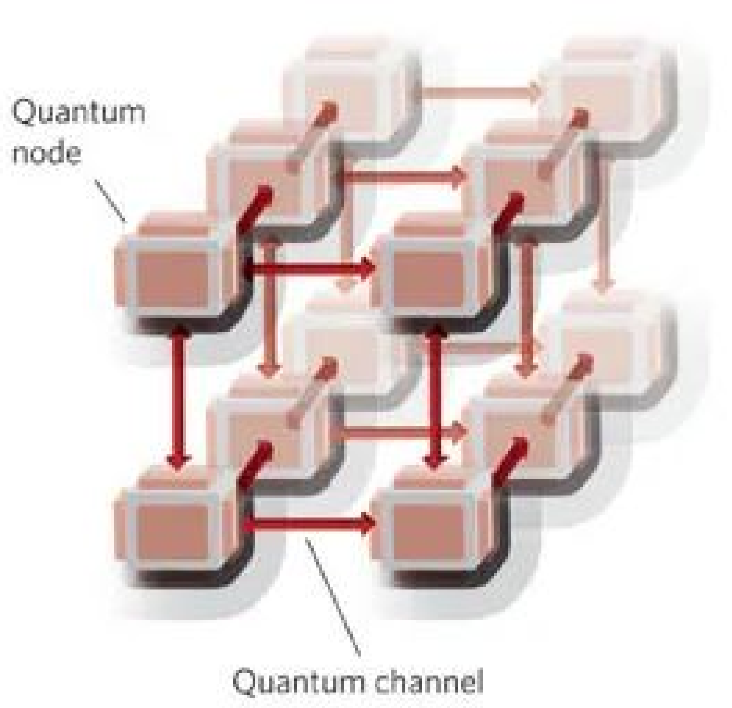

Figure 1.2 The Quantum Internet[2]

Dr Jeff Kimble in his pioneering work[2] envisioned an all-pervasive quantum internet consisting of quantum nodes which act as small-scale quantum processors connected by fully quantum channels. Such a form of quantum communication is achieved by the interaction between single photons and single atoms and by distributing the entanglement across the network using quantum teleportation. Over the past several years there has been progress in quantum processors, quantum memories, repeaters as well as quantum error correction. However, it is the need of the hour to develop robust and scalable systems that can deploy the grand vision of a fully quantum internet at scale.

1.3 Quantum Simulation

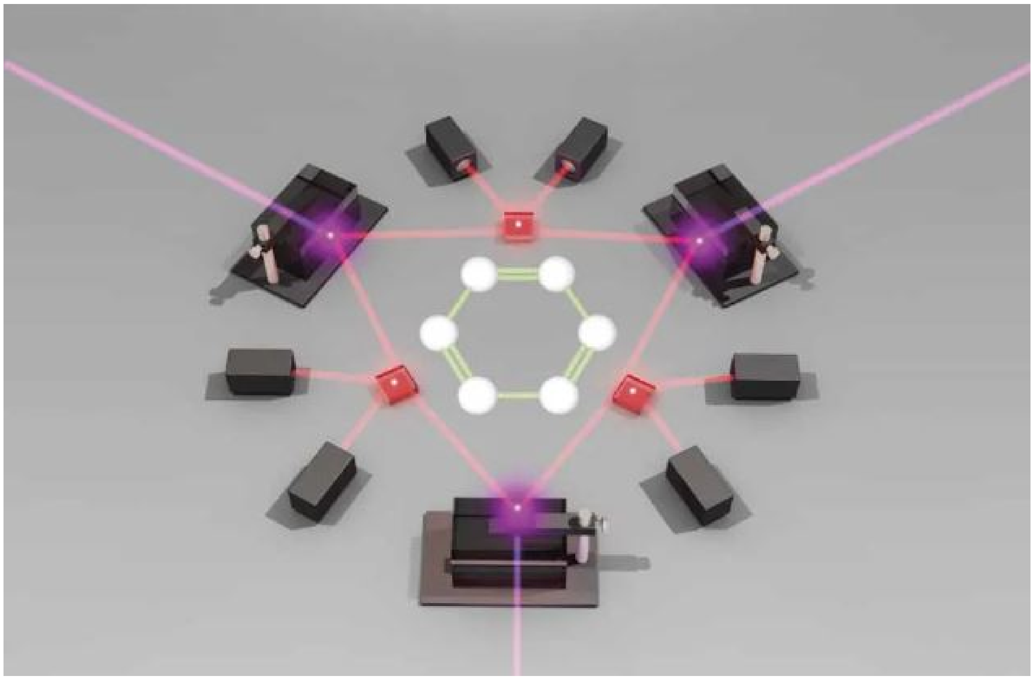

Figure 1.3 Photonic quantum simulation of a benzene molecule.[3]

Perhaps the most promising application of quantum photonics is in the field of quantum simulations. This is the area of physics where controllable coherent quantum photonic systems are built to mimick and study the evolution of complex many body quantum systems which are beyond the scope of classical computers. Figure 1.3 demonstrates the simulation of a benzene molecule[3] which is the most complex molecule that has been exactly simulated till date. This holds promise to potentially revolutionize the fields of quantum chemistry, drug design, quantum biology and solid state physics. In order to scale these simulations to useful large systems, it is necessary to integrate the key components of the simulator on chip.

1.4 Integrating Quantum Photonics On Chip

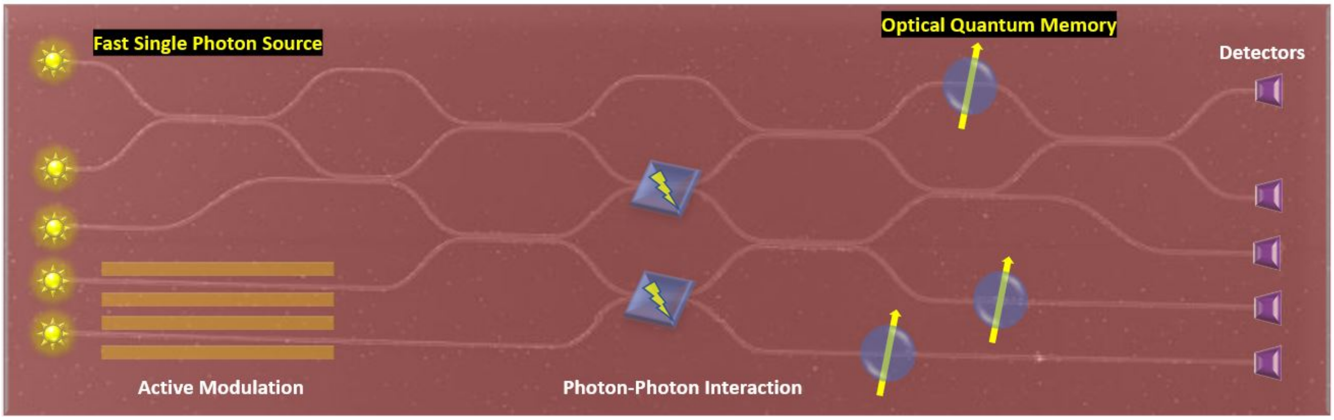

Figure 1.4 An integrated quantum photonic chip showing several key components in the quantum photonic toolbox.

Over the years the field of quantum photonics has progressed with rapid strides with several key proof of principle demonstrations across a wide variety of use cases as captured previously. To take the vision to the next level and create more robust, scalable, high bandwidth and efficient systems, it is necessary to integrate the key components of the quantum photonics toolbox on a chip scale platform. In this thesis, we focus on two of the more non-trivial components, a fast single photon source and an optical quantum memory.

Major Contributions

1. Demonstrated chip integrated routing of radiatively enhanced single photon emitters in two dimensional materials (Chapter 2)
    a. **S Dutta** et al. "Coupling quantum emitters in WSe2 monolayers to a metal-insulator-metal waveguide", **Appl. Phys. Lett.** *2018*, 113, 191105 (Chapter 2)
    b. T Cai, **S Dutta** et al., "Coupling Emission from Single Localized Defects in Two-Dimensional Semiconductor to Surface Plasmon Polaritons", **Nano Letters** *2017*, 17, 11, 6564-6568 (Chapter 2)
    c. **S Dutta** et al. "Coupling Single Defect Emissions From 2-Dimensional Semiconductors into Long-Range Propagating Gap Plasmons in Metal-Insulator-Metal Waveguides", **Conference on Lasers and Electro-Optics (CLEO)**, May 2018, San Jose, CA, USA. (Chapter 2)
2. Developed for the first time a new integrated photonic platform in thin film lithium niobate doped with rare earth ions (Chapter 3-5)
    a. **S Dutta** et al. "An Integrated Photonic Platform for Rare-Earth Ions in Thin-Film Lithium Niobate", **Nano Letters** *2020*, 20, 1, 741-747 (Chapter 3)
    b. **S Dutta** et al. "A Quantum Memory with Rare-Earth Ions in Thin-Film Lithium Niobate", Manuscript in preparation. (Chapter 4)
    c. **S Dutta** et al. "A Scalable Nanophotonic Platform for Rare Earth Ions" **American Physical Society (APS)** Meeting, March 2020, Denver, CO, USA (Chapter 3)

Outline

Chapter 1: Briefly introduces the scope of quantum photonics and highlights the need for integrating the different photonic components on a single chip scale platform.

Chapter 2: Introduces single photon emitters in 2D materials and demonstrates faster emission from integrated emitters on chip.

Chapter 3: Demonstrates a new integrated photonic platform consisting of rare earth ions in thin film lithium niobate and investigates the optical as well as coherence properties of the ions in the thin film.

Chapter 4: Demonstrates the first integrated optical quantum memory in thin film lithium niobate.

Chapter 5: Delineates progress towards an ideal quantum memory on chip with high efficiency as well as on-demand retrieval.

Appendix 1: Provides supporting information towards demonstrating a chip integrated single photon source.

Appendix 2: Provides supporting information towards demonstrating an integrated photonic platform for rare earth ions in thin film lithium niobate.

Chapter 2: A Fast Integrated Single Photon Source

2.1 2D Materials - An Emerging Single Photon Source

In recent years, defects bound excitons in two dimensional semiconductors have emerged as a new class of single photon emitters with ultra-narrow linewidths of 100 μeVs, as well as high single photon purity.[4–7] These emitters are located at the surface of an atomically thin monolayer which allows them to come in close proximity to photonic nanostructures. Another characteristic feature is that they can be deterministically induced by strain engineering allowing for site specific positioning.[8–10] Thus, with the ability to position these atomically thin quantum emitters, one can efficiently couple to the confined mode of optical nanostructures providing a platform for coherent light-matter interactions. Such a platform is critical for applications such as quantum communication and quantum information processing[2,11].

2.2 Surface Plasmons Are Great For Light Matter Coupling

2D materials with their narrow linewidths and flexibility in terms of positioning, offer a promising path to tailoring strong light matter interactions. However, apart from nanoscale positioning of emitters, the nanostructure must also exhibit a high optical density of states. A strong contender for the photonic nanostructures is surface plasmon polaritons generated at a metal-dielectric interface. Surface plasmons exhibit extreme subwavelength confinement of light[12,13] and an atom-like dipole emitter placed near the metal-dielectric interface, preferentially emits into the surface plasmon mode due to its high optical density of states.[14] The strong optical decay of emitters into the surface plasmon results in efficient coupling of emitters to a common plasmonic mode that can lead to strong photon-photon interactions.[15] Coupling also produces a significant enhancement in the rate of spontaneous emission of the emitters[14,16,17] which can help realize a fast single photon source on-chip. Thus, single photon emitters in 2D materials, coupled to surface plasmon polaritons establishes a platform for compact active photonic circuits essential for quantum information processing[18–20]. Several previous works reported deterministic coupling of quantum emitters with plasmonic nanocavities[21–23]. However, this does not result in a propagating surface plasmon polariton which is desirable for non-linear plasmonic circuit elements.

2.3 Coupling 2D Emitters With Silver Nanowires

We demonstrate that single defects in 2D semi- conductors can efficiently couple to surface plasmon polaritons. We deposited atomically thin WSe_2 sheets on colloidally synthesized silver nanowires. Localized, atom-like defects naturally form along the nanowire surface due to an induced strain gradient. Because of the proximity of the induced defects to the surface, they efficiently couple to propagating surface plasmon polaritons. We show an average coupling efficiency with a lower-bound of 26% ± 11% from the emitter to the silver nanowire. Such a coupled system could be used for applications such as ultrafast single-photon sources,[4,6] which paves a way toward super compact plasmonic circuits.

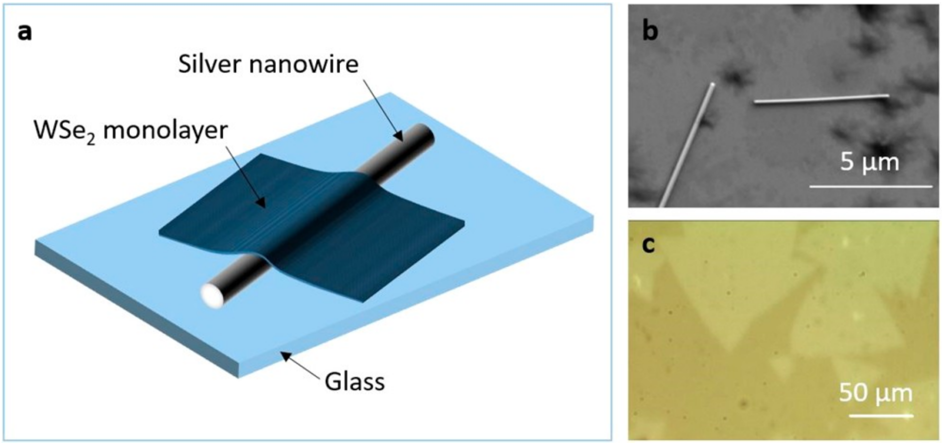

Figure 2.3.1. (a) The 3D schematic layout of a silver nanowire/WSe$_2$ monolayer device. (b) Scanning electron micrograph showing the silver nanowires used in the experiment. (c) Optical micrograph of WSe$_2$ monolayer flakes grown by chemical vapor deposition. Lighter areas correspond to the monolayer.

Figure 2.3.1a shows a schematic of the device. We first deposited chemically synthesized, bicrystalline silver nanowires[31,32] with average diameter of 100 nm and lengths varying from 3 to 10 µm, on a glass slide. Figure 1b shows a scanning electron micrograph (SEM) of the silver nanowires used in the experiment. We employed a dilute enough solution that the deposited nanowires were well separated, enabling us to isolate individual nanowires on an optical microscope. After depositing nanowires, we transferred a monolayer of WSe$_2$ sheets on top of the nanowires. Figure 2.3.1c shows a microscopic image of the WSe$_2$ monolayers used in the experiment. We synthesized these monolayers on a sapphire substrate using a chemical vapor deposition method[33] then transferred them to the glass slide using a polydimethylsiloxane (PDMS) substrate as an intermediate transfer medium.[34] We grew a high density of monolayer flakes on the substrate to ensure that the WSe$_2$ covered a large fraction of the nanowires after transfer.

To characterize the sample, we cooled it to 3.2 K in an attoDRY cryostat (Attocube Inc.). We performed photo- luminescence measurements using a confocal microscope. To excite the WSe$_2$ monolayer, we focused the laser on the sample surface using an objective lens with a numerical aperture of 0.8. By adjusting the collimation of the input laser we attained either a small, diffraction-limited spot that was used to excite a specific point on a nanowire or a larger spot that was used to excite the entire length of the nanowire. We excited the sample using a continuous-wave laser emitting at 532 nm. We used the same objective lens to collect the photoluminescence from the sample. Pump laser light was rejected using a long-pass optical filter. We used a half-wave plate and a polarizing beam splitter to selectively collect signal with a certain linear polarization and direct the collected signal either to a monochrome scientific camera (Rolera-XR, Qimaging, Inc.) for imaging or to a single- mode fiber that acted as a spatial filter. The single mode *fi*ber was used to deliver the signal to a grating spectrometer (SP2750, Princeton Instruments). A flip mirror could be used to direct the grating-resolved signal to a charge-coupled device camera (PyLoN100BR, Princeton Instrument) to measure emission spectra, or to a Hanbury Brown and Twiss setup for photon correlation measurements where a time-correlated single photon counting unit (PicoHarp 300, PicoQuant Inc.) correlates signals detected by two single photon counting modules (SPCM-AQRH, Excelitas Technologies Inc.).

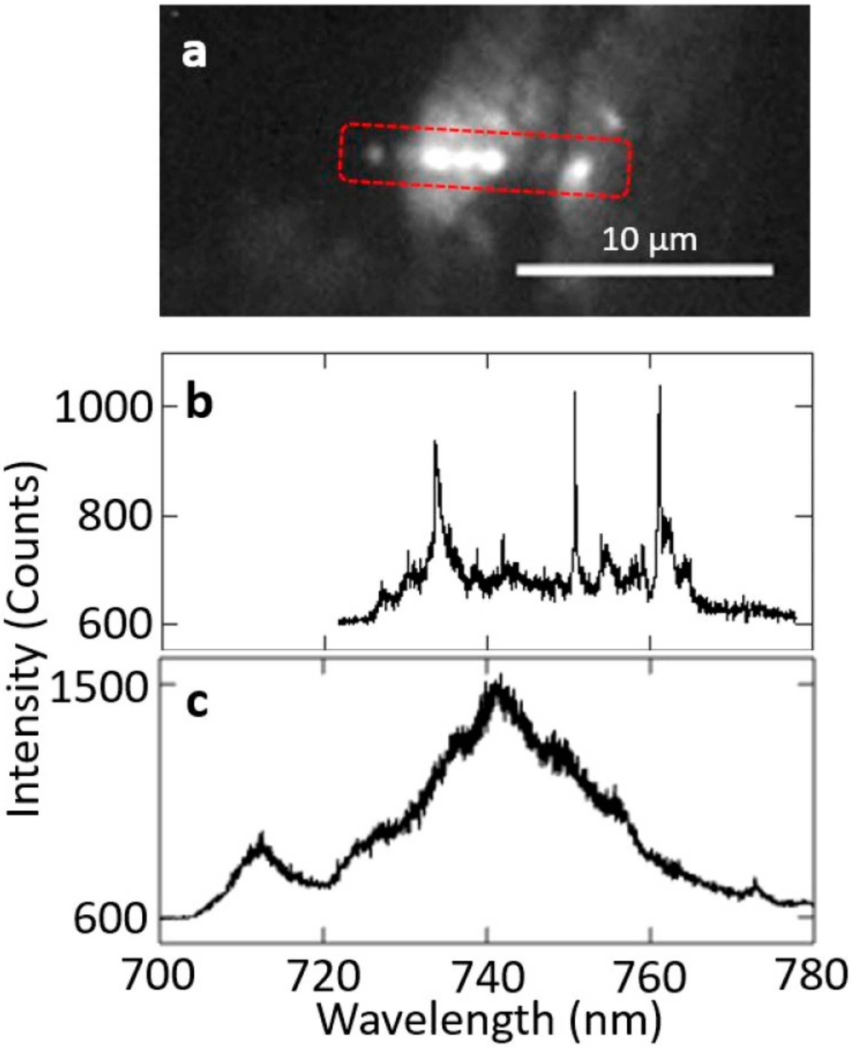

Figure 2.3.2. (a) Photoluminescence intensity map of a WSe_2 monolayer over a silver nanowire. The red box indicates the position of the silver nanowire. (b) Photoluminescence spectrum of the bright localized spots along the silver nanowire. (c) Photoluminescence spectrum of a bare WSe_2 monolayer.

Figure 2.3.2a shows a photoluminescence intensity map of a sample excited with the continuous-wave laser. The red box indicates the position of the silver nanowire. We used an uncollimated laser to generate a large focal spot that excited a large portion of the silver nanowire. In addition to diffuse photoluminescence from the entire excitation region, the image reveals bright localized emission spots along the length of the nanowire. Such localized emission has been reported to be signature of single localized emitters.[16–19] We found that these defects formed preferentially where the WSe_2 monolayer covered the nanowire. We attribute the formation of defects to strain induced by the nanowire. Similar strain-driven defect formation has been reported for patterned substrates that contained holes[23] or micropillars.[26]

To verify that the bright localized spots are single, atom-like emitters, we measured their emission spectrum. We used a large focal spot of the continuous-wave laser to excite multiple emitters along the wire and collected their photoluminescence. Figure 2b shows the resulting photoluminescence spectrum, which exhibits several sharp emission lines. The spectrum from the region containing the localized defects is distinct from the spectrum collected at a bare WSe_2 monolayer area, which displays two broad peaks corresponding to the exciton and ensemble of defects and impurities of the monolayer (Figure 2.3.2c). The sharp spectral emission at the bright localized regions supports the assertion that these spots are single, strain-induced emitters.

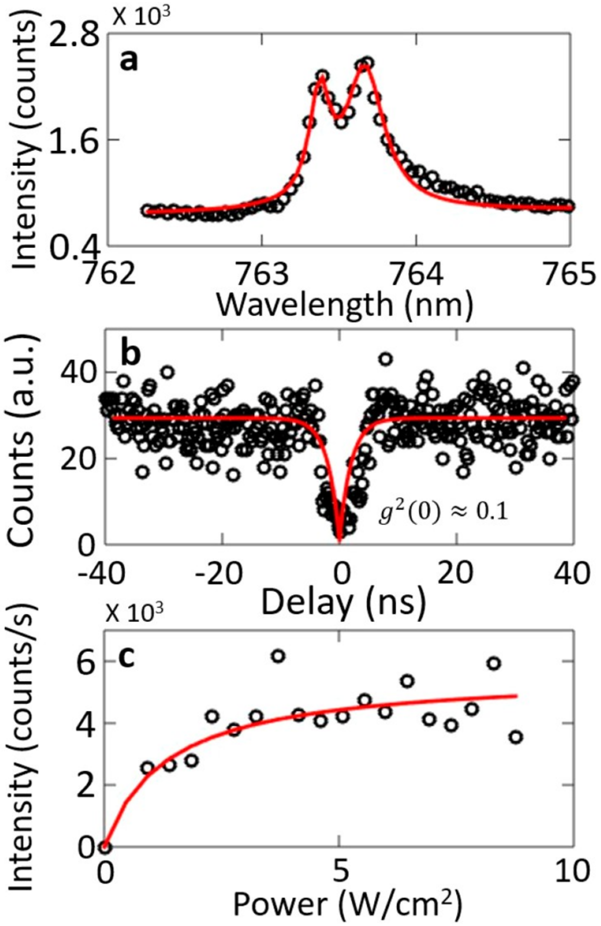

Figure 2.3.3. (a) Photoluminescence spectrum of a localized emitter(black circles) fitted with two Lorentzian functions (red curve). (b) Second-order correlation measurement of the emitter (black circles) fitted with a double exponential decay function (red curve). (c) The integrated photoluminescence intensity of a single emitter as a function of excitation power (black circles) shows a saturation behavior (red curve).

Figure 2.3.3a shows the spectrum of a representative single emitter along a nanowire. The emitter was excited using the continuous-wave laser with a highly focused spot, and the spectrum was obtained over a narrow spectral range. The spectrum is a doublet, each peak of which corresponds to one of two orthogonal linear polarizations of the emission. A fit of the spectrum to two Lorentzian functions gives line widths of 0.2 nm (456 μeV) for the peak at 763.4 and 0.3 nm (684 μeV) for the peak at 763.7 nm with a splitting of 0.3 nm (684 μeV).

This spectrum is similar to that of those natural, defect-bound, localized emitters observed previously in WSe_2 mono-layers.[16–19] We confirmed the single photon emission of the emitter shown in Figure 2.3.3a by performing a photon-correlation measurement. Figure 3b shows the second-order correlation measurement under continuous-wave excitation. Fitting the measured data with a double exponential decay function gives a $g^2(0) \approx 0.1$. This is well below the threshold of photon antibunching ($g^2(0) = 0.5$), which confirms that the emission originated from a single emitter. From the fit we also obtained a lifetime of the emitter to be 2.0 ns, which is consistent with previously measured lifetimes[16–19] and significantly longer than that of the excitonic emission of an WSe_2 monolayer, typically on the order of a few picoseconds at 4K.[35,36] We note that due to the large fluctuations in emitter lifetimes, we cannot infer a change in the radiative decay rate of the emitter from the lifetime.

Figure 2.3.3c shows the integrated intensity of the photo- luminescence of the same emitter in Figure 2.3.3a as a function of excitation power of the continuous-wave laser. The saturation behavior observed is consistent with single-defect emission. The solid line is a fit to a saturation function of the form $I = I_{\mathrm{sat}}P/(P_{\mathrm{sat}} + P)$, where I and I_{sat} are the integrated intensity and the saturation intensity, respectively, and P and P_{sat} are excitation power and saturation power, respectively. From the fit we determined a power of 1.3 W/cm^2 (before the objective lens) and an integrated intensity of 5.6×10^3 counts/s on the spectrometer at saturation.

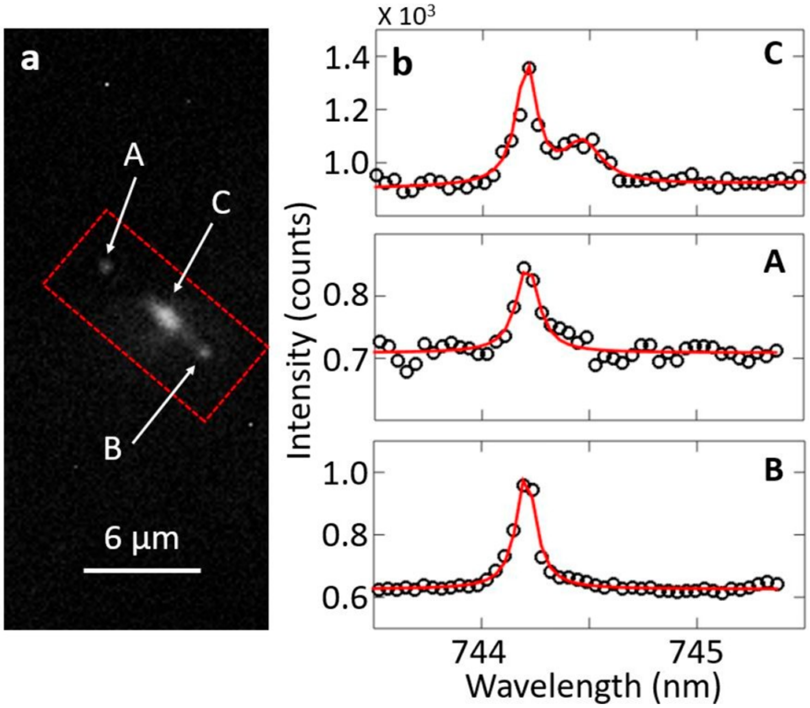

Figure 2.3.4. (a) A photoluminescence intensity map shows emission at the emitter (denoted “C”) and at both ends of the silver nanowire (denoted “A” and “B”). The red box indicates the position of the silver nanowire. (b) Photoluminescence spectra collected at “C” (top panel), “A” (middle panel) and “B” (bottom panel).

One fortuitous advantage of the strain-driven formation process is that the emitters are naturally generated near the high-field region of the wire. We therefore expect the emitters to couple efficiently to guided surface plasmon modes. Figure 4a shows a photoluminescence intensity map of an emitter near the midpoint of a silver nanowire. We focused the continuous- wave laser on the emitter at the location denoted “C”. In addition to the photoluminescence from the emitter itself, we also observed emission from both ends of the silver nanowire (denoted “A” and “B”). We attribute the light at the ends of the nanowire to emission from the emitter that couples to guided surface plasmon polaritons and travels to the ends. To verify that the emission at the wire ends originates from the defect, we measured the emission spectrum at all three points (Figure 2.3.4b). When we directly collected emission from the emitter at “C”, we observed a doublet, whose peaks corresponded to two orthogonal linear polarizations.[16–19] We fit the spectrum with two Lorentzian functions and arrived at two peaks centered at 744.2 and 744.5 nm with line widths of 0.1 and 0.2 nm, respectively. The collected emission from the ends of the silver nanowire shows only a single peak exhibiting linear polarization parallel to the silver nanowire. Fitting the single peak to a Lorentzian function gives a resonance of 744.2 nm and line width of 0.1 nm, which lines up with the shorter- wavelength peak of the doublet. We attribute the coupling of only one peak to the wire to the polarization selection of the guided surface plasmons of the silver nanowire. In this particular case, one peak aligns with the preferred polarization of the wire and the other does not, leading to different coupling efficiencies. Here our collection of polarization was not perfectly parallel to the wire so we were able to observe a doublet when we directly collected emission from the emitter at “C”. When we moved the collection spot away from locations A, B, or C, the observed peaks corresponding to the emitter quickly disappeared. Furthermore, when we moved the excitation spot away from the emitter, the peaks also disappeared, verifying that the emission originates from the localized defect.

To explore how well the single-defect emitters couple to the silver nanowires, we performed measurements on 21 different silver nanowires. We found that the average number of emitters generated per wire was 3.2. A portion of these emitters formatted sufficiently far away from the wire ends so we can well resolve them and the wire ends. Among these emitters, 33% of them exhibited coupling to the wires. We can estimate the coupling efficiency of the defect emission into the plasmonic mode of the silver nanowire by comparing the emission intensity at both ends of the nanowire to the overall emission of the emitter. To collect the emission intensities, we aligned the polarizing optics in our setup in such a way that we selectively collected linear polarization parallel to the silver nanowire. The coupling efficiency is given by

$$D = (I_A + I_B + L)/(I_A + I_B + I_C + L) \quad (2.3.1)$$

I_i (i = A, B, or C) is the integrated intensity collected at location i and L is number of photons lost while propagating along the silver nanowire. Equation 2.3.1 assumes that the collection efficiency of the emission at the three locations are the same. Although each emission spot originates from a subwavelength source, simulated far-field emission patterns show that the end of a wire tends to direct emission to the side rather then the top, leading to a lower collection efficiency compared to that of an emitter at the middle of a wire. This reduced efficiency indicates that we are in fact under-estimating the coupling efficiency. Because we do not have an accurate means of measuring L, we assume $L = 0$, which further underestimates the coupling efficiency.

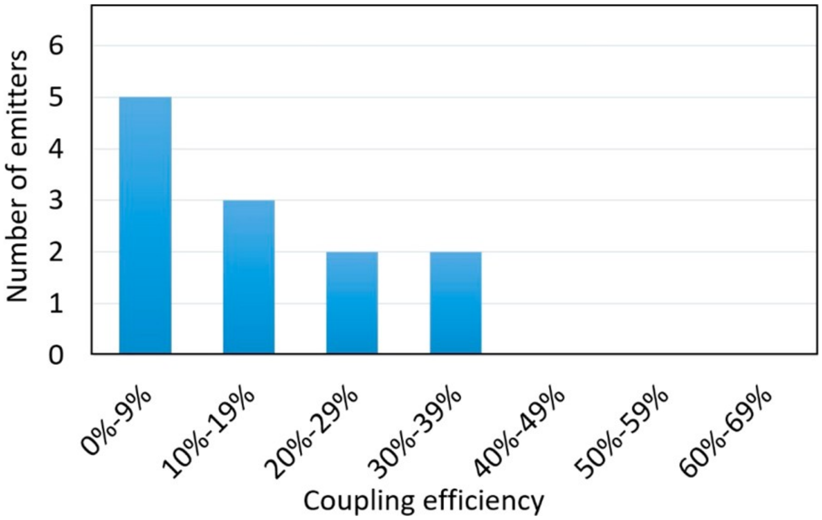

Figure 2.3.5. Distribution of the coupling efficiencies of single-defect emitters to the silver nanowires.

Figure 2.3.5 shows the distribution of the coupling efficiencies of the coupled emitters.

We measured an average coupling rate to the wire of 26% ± 11%. The variation of the coupling efficiencies originates from multiple factors such as variations in the proximity of the emitters to the surface of the silver nanowires, loss of the silver nanowires, and fluctuations in the shape of the ends of the silver nanowires.

2.4 Local Field Overlap Is Critical For Faster Emitters

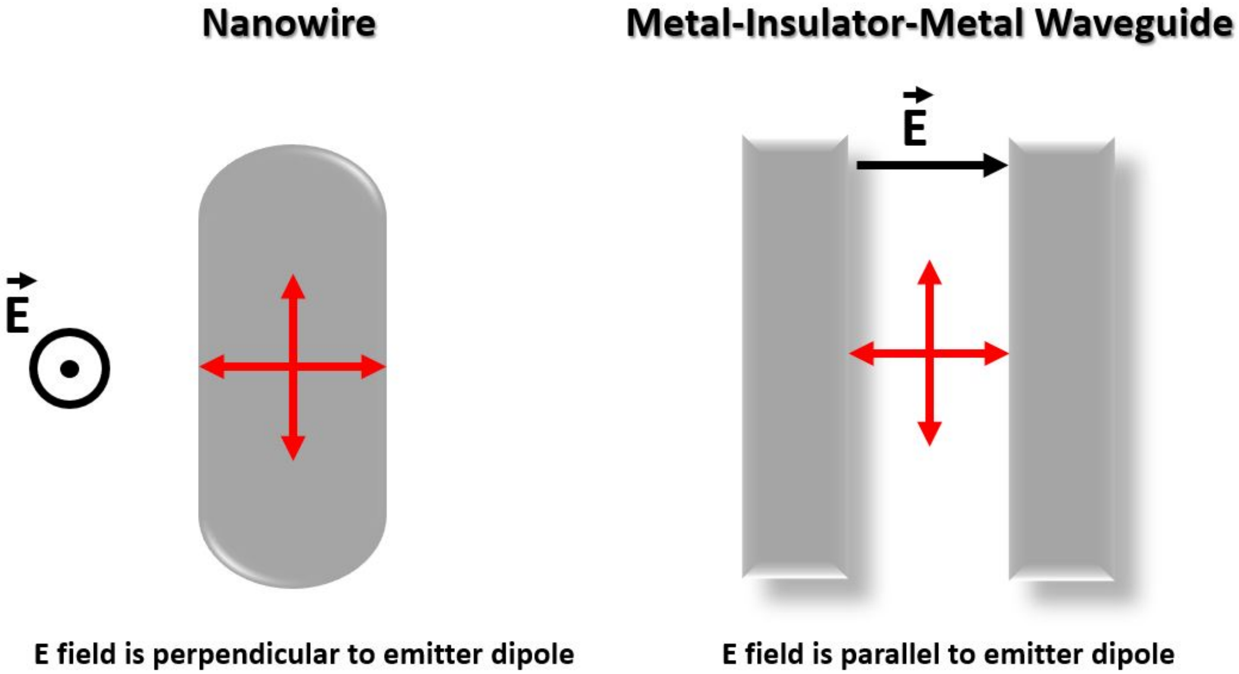

Figure 2.4 Schematic showing that the emitter dipole (red vector) is perpendicular to the local electric field (black vector) for the nanowire geometry and parallel to the same for a metal insulator metal geometry.

We have demonstrated efficient coupling between a localized emitter in atomically thin WSe_2 and the propagating surface plasmon mode of a silver nanowire. However, we do not observe an enhancement in the rate of radiative emission. This is because the emitter dipole in the 2D material is in plane and the local electric field of the surface plasmon mode is always perpendicular to the metal surface. In case of the nanowire geometry the local electric field points radially outward and the emitter dipoles point tangential to the metal nanowire surface. Hence, there is very little scope for overlap in this geometry as shown in Figure 2.4. However, in case of a metal insulator metal structure, the electric field is confined in the gap region and aligns up with one of the emitter dipoles. Such a geometry thus holds significant promise for radiative enhancement as well as on chip light guiding.

2.5 Coupling 2D Emitters With Metal Insulator Metal Waveguides

We show coupling of single emitters in WSe_2 with propagating surface plasmon polaritons in silver-air-silver, MIM waveguides. The strain gradient enforced on the monolayer by the waveguide generates sharp localized single photon emitters close to the plasmonic mode. The component of the in-plane dipole moment perpendicular to the metal surface preferentially couples to the travelling waveguide mode, leading to a Purcell[24] enhanced emission with an average Purcell factor of 1.9. A single emitter in a 2D material coupled to an MIM waveguides can lead to deterministic active plasmonic circuits that can be lithographically fabricated on chip.

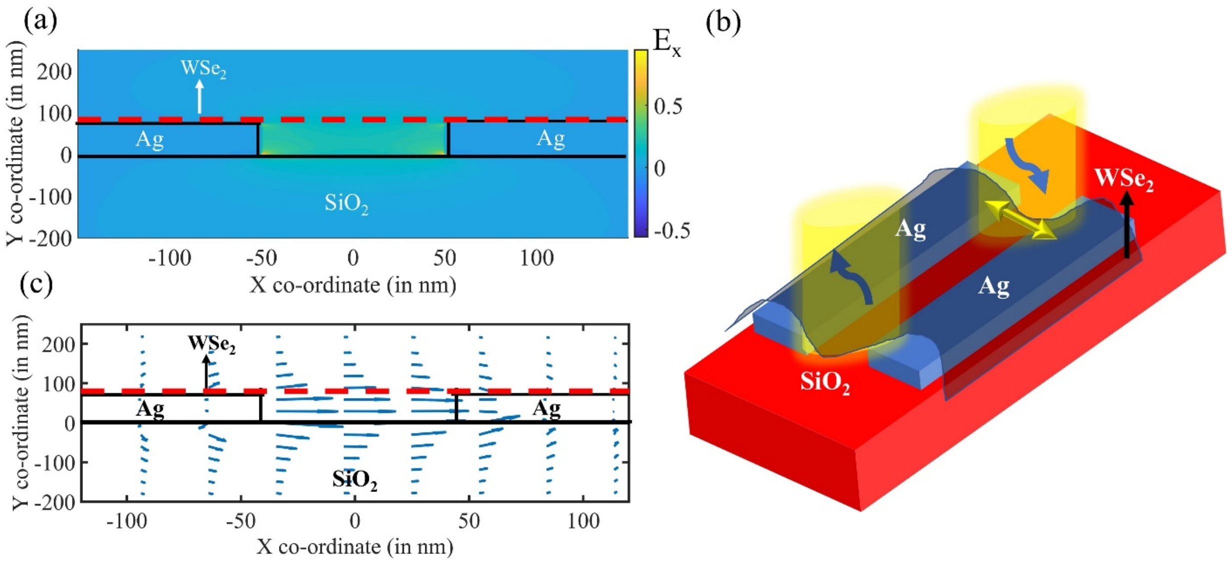

Fig. 2.5.1. (a) Finite Difference Eigenmode simulation (Lumerical Inc.) showing the X component of the electric field for the surface plasmon mode propagating along the Z axis in the MIM waveguide. (b) Schematic of an MIM waveguide covered by a WSe_2 monolayer. The yellow dipole represents a quantum emitter in WSe_2. The blue arrows denote the excitation and collection points respectively. (c) Finite Difference Eigenmode simulation (Lumerical Inc.) showing the vector plot of the electric field in the gap region of the MIM waveguide.

Fig. 2.5.1(a) shows a finite difference eigenmode simulation for the surface plasmon mode in a silver-air-silver MIM structure. The simulation is performed using the commercial software, Lumerical MODE Solutions. We refer to the Palik model[25] for the silver films used in our simulations of the waveguide mode. The color map represents the magnitude of the electric field (E_x) vector of the plasmon polariton mode, directed along the X axis which is oriented in the in-plane direction with respect to the monolayer. Fig. 2.5.1(c) plots a vector map of the electric field showing a strong localization along the X axis in the air gap region between the two metal strips of the MIM waveguide. Because the monolayer dipole moment is in-plane, it can align to the electric field orientation of the waveguide. This contrasts with nanowire waveguides where the preferred dipole orientation is radial to the structure and always orthogonal to the plane of the monolayer, hampering coupling efficiency.

We fabricate the MIM waveguides using electron beam lithography, followed by metal deposition and liftoff. We spin coat Si/SiO_2 sample with ZEP520A ebeam resist at 4500 rpm and post bake it for 5 min at 180° C. Next, we pattern the samples using an electron beam lithography system at an acceleration voltage of 100 kV (you can cite the exact ebeam model here in parenthesis if you want), using a dose array ranging from 250 to 480 $\mu C/cm^2$. We develop the resist in n-Amyl Acetate (ZED-N50), Methyl isobutyl ketone and Isopropyl alcohol for 1min, 30s and 30s respectively. For the metal evaporation step, we use a thermal evaporator to deposit 5nm and 65nm, Cr and Ag at evaporation rates of 5 A/s and 130 A/s, respectively to achieve high quality plasmonic films.[26] We perform liftoff by soaking in acetone overnight and subsequently rinsing with Acetone and Isopropyl alcohol . The fabricated waveguides have gaps ranging from 90 nm to 110 nm and a length of 7 μm, Fig. 2(a). After waveguide fabrication, we transfer the monolayer samples onto the MIM structures. We grow WSe_2 monolayers on a sapphire substrate using a chemical vapor deposition method[27] and then dry stamp them on the MIM sample using a polydimethylsiloxane (PDMS) gel as an intermediate transfer medium.[28]

To characterize the sample, we cool it to 3.2 K in closed cycle cryostat (Attocube Inc.) and perform photoluminescence measurements using a confocal microscope geometry. We use a continuous wave excitation laser emitting at 532 nm to perform photoluminescence spectroscopy. We focus the laser onto the sample surface with an objective lens (Numerical aperture 0.7) to excite a small diffraction limited spot on the MIM waveguide. A 700 nm long-pass optical filter rejects the pump wavelength to isolate the fluorescence signal. A monochrome scientific camera (Rolera-XR, Qimaging, Inc.) images the fluorescence field pattern. Alternately, we use a grating spectrometer (SP2750, Princeton Instruments) to measure the fluorescence spectrum.

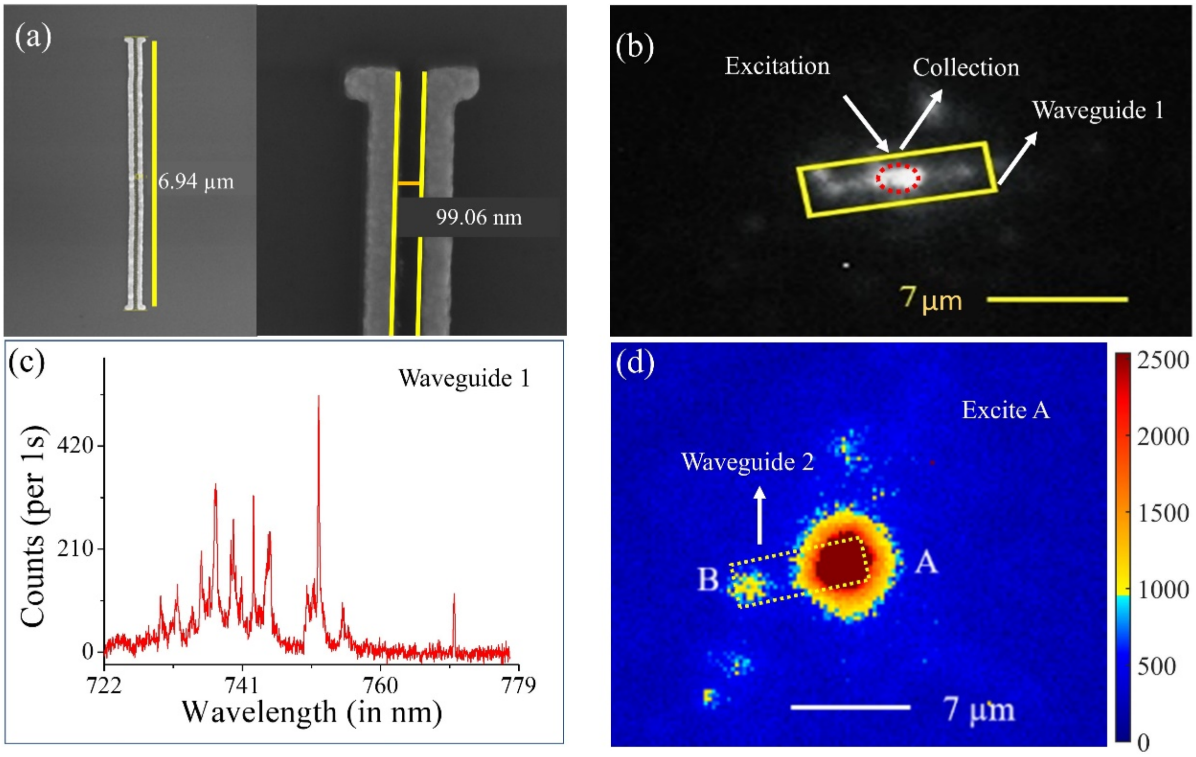

Fig. 2.5.2. (a) SEM image of a representative MIM waveguide showing the length and gap width. (b) Shows a photoluminescence intensity map of a WSe_2 flake located on top of a waveguide marked by the yellow box. (c) Photoluminescence spectrum collected at the point on the waveguide marked by the dotted circle in (b), showing multiple defect emissions structurally aligned with the waveguide. (d) Photoluminescence intensity map showing a representative flake/waveguide system while exciting a coupled defect located at one end A of a waveguide. The defect at A couples to the waveguide and is scattered off at B causing the bright feature.

Fig. 2.5.2(b) shows the photoluminescence map of the flake/waveguide system as observed on the camera. We observe bright localized emission spots in the vicinity of the waveguide. The photoluminescence spectrum, Fig. 2.5.2(c) of the bright spot as marked in Fig. 2.5.2(b) (dotted circle) shows the presence of several sharp peaks corresponding to single defects emitters in WSe_2.[4–7] These emitters arise from the strain gradient affected on the monolayer by the MIM waveguide. Such strain-induced defect formations have been previously shown in monolayers suspended over holes or placed on top of nanopillars and nanowires.[8,10,29] We further observe bright spots at the ends of the waveguide. We assert that the emission from these single defects couple to the propagating surface plasmon polariton in the waveguide and scatter of the ends as photons resulting in such bright spots.

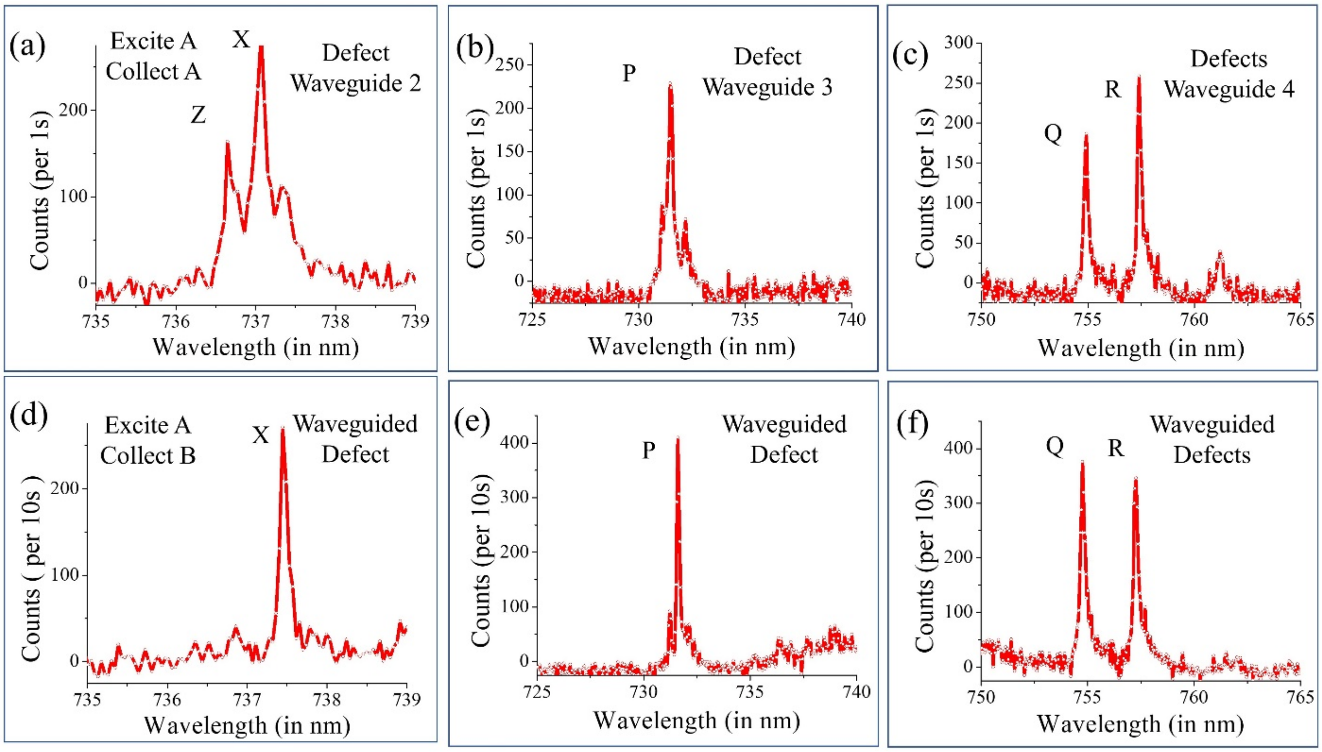

Fig. 2.5.3. (a), (b), (c) Shows the photoluminescence spectra of four different coupled defects (X, P, Q and R) with the excitation and collection spots aligned to the same point, at one end

of three different waveguides. (d), (e), (f) Shows the photoluminescence spectra of the waveguide defects (X, P, Q and R) with the excitation spot fixed at the location of the defect and collection spot moved to the far end of the waveguide.

To verify the assertion of coupling, we search for defect emissions at one end of the waveguide while looking for the scattered emission at the other end. Fig. 2.5.2(d) shows a representative camera image of the fluorescence intensity when we excite point A at one end of a waveguide (Waveguide 2). Fig 2.5.3(a) shows the photoluminescence spectrum with both the excitation and collection spots focused at A. We observe two resolvable peaks at 736.6 nm and 737.1 nm which are labelled as Z and X, respectively. We fit the peaks to a Lorentzian to determine linewidths of 0.17 nm (Z) and 0.10 nm (X). These peaks constitute a set of orthogonally polarized doublets.[4–7] (Appendix Fig. A1.3) Keeping the excitation at the location of the defect (end A) we move the collection spot to the far end of the waveguide (end B) and collect the corresponding spectrum, Fig 2.5.3(d). This time we observe only one of the doublet peaks, X at 737.4 nm since only one of the two cross polarized peaks aligns with the direction of the electric field of the surface plasmon polariton. The peak vanishes when we move the excitation spot away from A. We observe a small redshift of 0.3 nm in the wavelength of the waveguided peak, X. To further understand this phenomenon, we measure similar spectra for three other coupled defects, P, Q and R on two different waveguides, Waveguide 3 and Waveguide 4 respectively. Fig 2.5.3(b) and (c) show the spectra of defects P, Q and R when both the excitation and collection are aligned to one end of waveguides 3 and 4 respectively. Fig 2.5.3(d) and (e) show the spectra of the scattered defects when we move the collection point to the far end of the waveguides keeping the excitation at the same point. We observe a 0.11 nm redshift for defect P and a 0.15 nm blueshift for both defects Q and R when looking at the scattered spectra. We conclude that these small and consistent deviations are due to spectral wandering of the defect peaks in time over the course of the measurement. Indeed previous literature reports spectral wandering of upto 1 meV for such defects in WSe_2.[4–7] To further ensure that the emission we see is not due to the pump coupling to the waveguide and exciting a different defect at the other end, we move the excitation away from the location (A) of the defect and directly excite B in waveguide 2, measuring the emission at B. The spectrum shows the background photoluminescence emission from the monolayer flake and does not show the sharp quantum dot like feature. (Detailed discussion in Appendix Fig. A1.4)

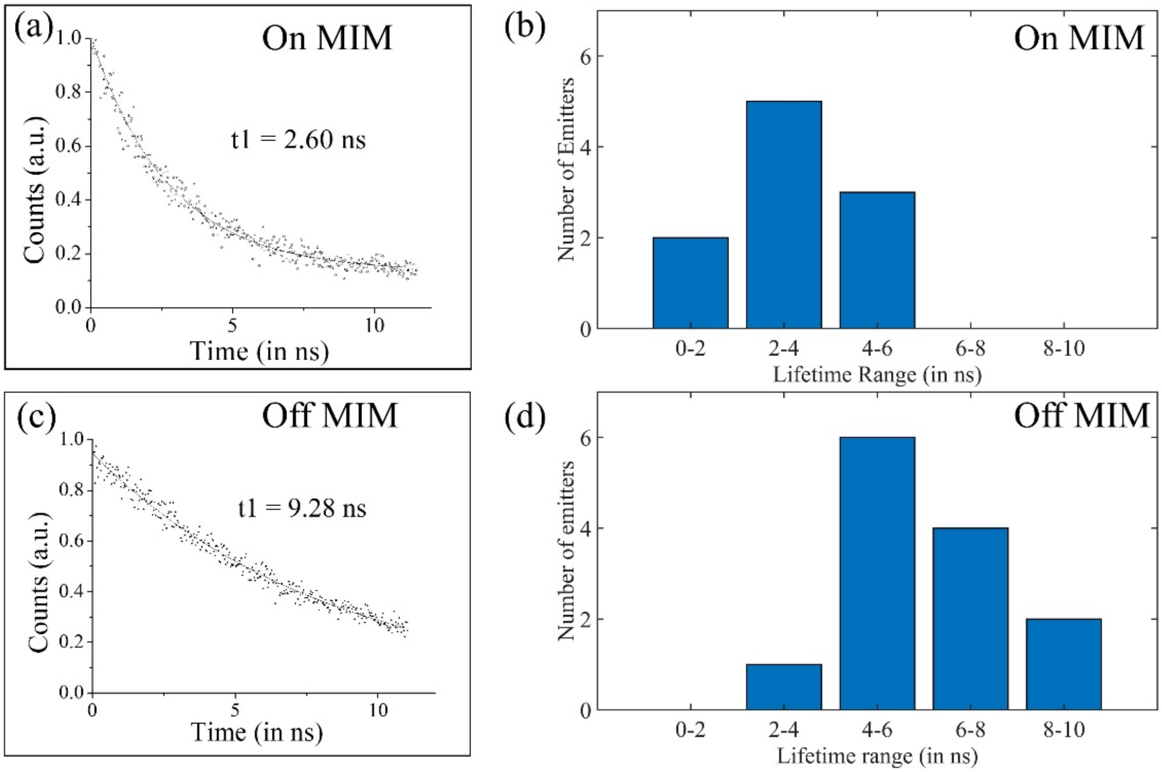

Fig. 2.5.4. (a) Lifetime of a representative emitter located on the MIM waveguide. (b) Lifetime statistics of emitters located on the waveguide. (c) Lifetime of a representative emitter located away from the MIM waveguide. (d) Lifetime statistics of emitters located far from the waveguide.

Spontaneous emission enhancement is a strong signature of efficient coupling of dipole emitters to optical nanostructures. But measuring radiative enhancement in WSe_2 emitters is complicated by the fact that even in pristine monolayer, the radiative lifetimes are broadly distributed and can range from 3 ns to as long as 19 ns.[23] To explore Purcell[24] enhancement, we therefore accumulate statistics over a total of 23 emitters, with 10 emitters located on the waveguide/monolayer system and 13 emitters located on the pristine monolayer, away from the waveguide. The lifetime measurements are carried out with the excitation and collection spots aligned at the same point, the location of the defect. The distributions of the radiative lifetimes for the two sets of emitters are plotted in Fig. 2.5.4(b) and (d). We see a clear decrease of the lifetimes for the emitters that are located on the MIM waveguide. The radiative lifetimes of the emitters are fitted to a Gaussian. We find that the emitters on the waveguide have an average lifetime of 3.19 ± 1.12 ns while those off the waveguide have an average lifetime of 6.00 ± 0.94 ns. Thus, we can identify two distributions with distinctly resolvable means. From these values we determine an average Purcell[24] enhancement of 1.9 for near-field coupling of the single emitters to the MIM waveguides.

In conclusion, we showed coupling of single emitters in WSe_2 with propagating surface plasmon polaritons in MIM waveguides. The strain gradient enforced on the monolayer by the waveguide generated localized single photon emitters close to the plasmonic mode. The coupled emitters experienced an enhancement in the radiative lifetime measured by the average Purcell[24] factor of 1.9. Our results can realize a fast, integrated single photon source by coupling the MIM structure with a dielectric waveguide.[30,31] It is however, necessary to gain better control over the coupling strength between the emitter and the plasmonic mode. One approach might be to engineer better quality of defects by reducing the non-radiative relaxation in the system by encapsulating the monolayer by boron nitride layers[32] which is known to decrease the linewidths of the defects. With better control over the coupling strength one can think of more appealing applications that harp on the giant non-linearity presented by the plasmon-emitter system. The saturable two-level system of the emitter absorbs and subsequently scatters off single photons while being invisible to the next photon. This can realize a single photon switch.[20] Thus, combined with recent advances in the fabrication quality of 2D monolayer,[32] our results present a versatile platform which can lead to compact active plasmonic circuits on chip.

Chapter 3: An Integrated Photonic Platform For Rare Earth Ions In Thin Film Lithium Niobate

3.1 Rare Earth Ions – A Review

Rare-earth ion dopants are solid-state emitters that have found widespread uses in both classical and quantum optics[33–36]. These emitters exhibit stable optical transitions with long lifetimes, making them a useful gain material for lasers and optical amplifiers[36,37]. They also feature narrow homogeneous linewidths,[38,39] which find broad applications in optical signal processing as high finesse filters for laser phase noise suppression,[36,40] and medical imaging[41]. Due to their long coherence times[42], rare-earth ions are also promising candidates for optical quantum memories[43] and qubits[44], which are essential components of quantum networks[2] and distributed quantum computers[45].

3.2 Rare Earth Ions Integrated Photonics

The incorporation of rare-earth ions into integrated photonics could enable a new class of active opto-electronic systems with applications in classical and quantum information processing. Integrated photonics combines many optical components on a compact chip, which is essential for scalability and device efficiency. However, incorporating rare-earth ions into integrated photonic devices has proved challenging because these emitters typically reside in bulk crystals[33,36,40], which are not compatible with conventional planar fabrication techniques[46]. One effective solution is to directly pattern integrated photonic devices into the bulk either by ion milling[47–49] or by ion diffusion to form waveguides[33,50]. Hybrid integration[51–53], where nanostructures are evanescently coupled to rare-earth ions in the bulk, provides another promising approach. Implanting rare-earth ions into materials that are compatible with planar fabrication, such as Er^{3+} implanted in silicon nitride[54,55], has been demonstrated, but the homogeneous linewidth is broadened even at cryogenic temperatures[55,56]. A thin film material platform that is single crystalline and preserves the bulk properties of the emitter is therefore critically lacking.

3.3 Thin Film Lithium Niobate

Lithium niobate provides a promising host material for rare-earth ion integrated photonics[33]. Rare-earth doped channel waveguides in lithium niobate have been used to realize lasers[57,58] and quantum memories[50,59,60] spanning a vast range of wavelengths from the infrared to the telecom band. Furthermore, lithium niobate is compatible with commercial wafer scale smart-cut which enables thin single crystalline films on oxide, a lower index material that can support low loss waveguides[61] and also act as a sacrificial layer[62,63]. But the properties of rare-earth ions in smart-cut thin films have not yet been carefully explored.

3.4 Rare Earth Ion Doped Thin Film Lithium Niobate

We demonstrate an integrated photonic platform for rare-earth ions in a single crystal lithium niobate thin film which is compatible with scalable top down fabrication. The material stack is composed of smart-cut thin films of Thulium (Tm^{3+}) doped lithium niobate and wafer bonded onto silicon dioxide grown on a undoped lithium niobate substrate. Using this substrate, we pattern waveguides in the Tm^{3+} doped thin film and show strong optical absorption and spectral hole burning through waveguide transmission measurements. We compare the optical properties of the rare-earth ions in the waveguides to those in the bulk and find them to have virtually identical lifetimes and emission spectra, despite significant processing involved in smart-cut and patterning of the thin film. Furthermore, the smart-cut process induces negligible background emission in the substrate. Due to the small cross-sectional area of the waveguides patterned in a thin film, we are able to burn narrow spectral holes with powers that are over two orders of magnitude lower than in previously reported titanium in-diffused waveguides[59]. These results demonstrate the suitability of these emitters for stable and spectrally narrow optical quantum memories, lasers, and filters in a thin film material that is compatible with wafer-scale processing and fabrication.

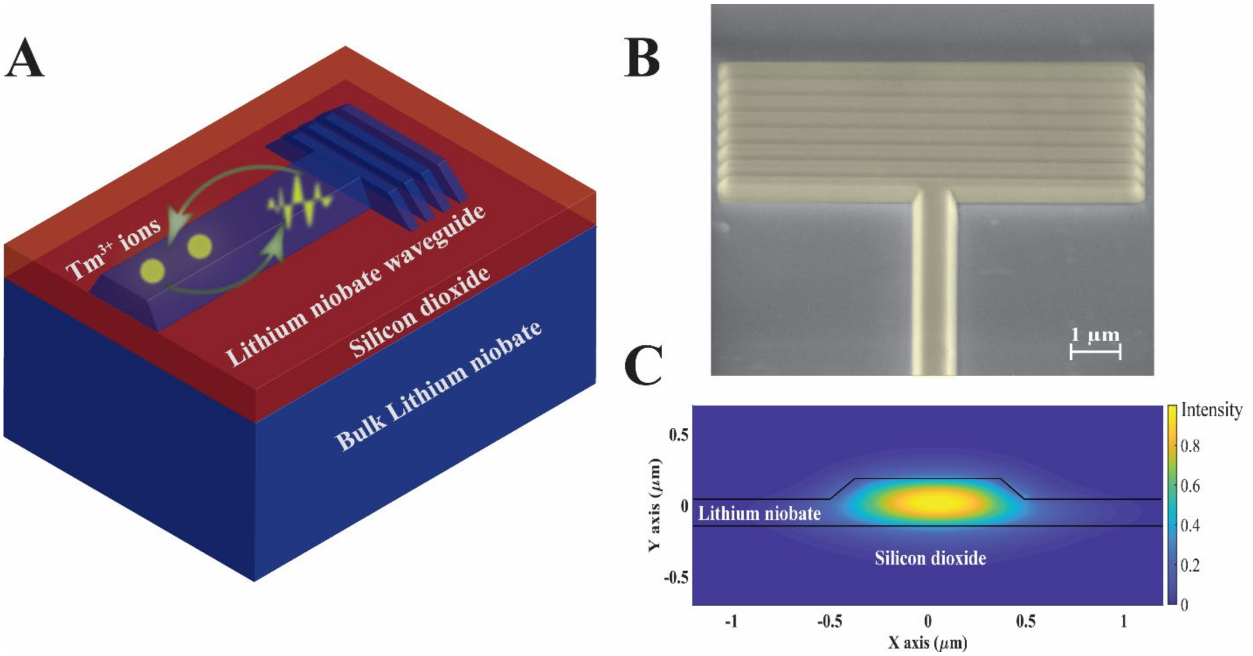

Figure 3.4.1. (A) Device geometry. Schematic of the cross-section of a waveguide etched in the heterogeneous material stack. (B) Scanning Electron Microscopy image of the waveguide with grating couplers patterned in the Tm^{3+} doped lithium niobate thin film. (C) Finite Difference Time Domain simulation showing the electric field distribution along the waveguide cross-section.

Fig 3.4.1(A) shows a schematic of the layer structure of the fabricated device. We begin with a bulk X-cut lithium niobate substrate doped with 0.1% Tm^{3+}. Using a commercial smart-cut process (NANOLN), we fabricate a 300 nm layer of doped single crystal lithium niobate wafer bonded to a 2 µm thick layer of silicon dioxide grown on undoped bulk lithium niobate as the substrate material. We etch waveguides into the doped thin film using a two-layer electron beam lithography and dry etching process (see Methods). Fig. 3.4.1(B) shows a scanning electron microscope image of the fabricated waveguide along with grating couplers to couple light from the out of plane dimension. The waveguides have smooth sidewalls etched at an angle of 45 degrees. We select the waveguide geometry to be single mode at 794 nm which is the $^3H_6 \rightarrow ^3H_4$ optical transition for the Tm^{3+} ions. Fig. 3.4.1(C) shows a finite difference time domain simulation of the electric field intensity inside the waveguides for the fundamental TE mode at this wavelength. The waveguides are 700 nm wide and constitute only a partial etch of the thin film with an etch depth of 125 nm. Such a design minimizes the interaction of the light with the etched sidewalls resulting in low propagation losses[61]. The optical mode exhibits transverse area of (176 nm X 400 nm) 0.07 μm^2, which is over 2 orders of magnitude smaller than titanium in-diffused waveguides[59]. The mode is tightly confined in the thin lithium niobate film where it interacts with the Tm^{3+}. The direction of the waveguide must be selected carefully so that the TE mode of the waveguide aligns with the dipole moment of the ions, which are oriented perpendicular to the optical axis (*c* axis) of the lithium niobate substrate [50,59,64]. For comparison, we fabricated waveguides that are both parallel and orthogonal to the *c* axis.

To pattern the thin film waveguide we first grow a 500 nm layer of amorphous silicon which acts as a hard mask. We spin a 300 nm layer of ZEP520A and pattern the samples using a 100 kV electron beam lithography system (Elionix). We deposit 10 nm chromium in an electron beam evaporator and perform metal liftoff to make a negative mask. Using chromium as a mask we first etch the silicon with a standard fluorine chemistry dry etching recipe. Now, with the silicon as a hard mask we transfer the pattern to the thin film lithium niobate using an optimized argon plasma physical etching technique. Finally, we use a 30% solution of KOH at 80° C to remove the remaining silicon. We grow a 2 μm layer of oxide on top of the waveguides to reduce scattering induced losses at the waveguide sidewalls.

To characterize the sample, we cool it down to 3.6 K in closed cycle cryostat (Attocube attoDRY). We use a confocal microscope with a diffraction limited spatial resolution between the excitation and the collection spots to perform photoluminescence and transmission measurements through the thin film waveguides. To perform broadband measurements, we excite the sample with a supercontinuum source (NKT Photonics) and detect the signal using a spectrometer (Princeton Instruments). For time-resolved measurements and spectral hole burning we use a single frequency laser (M Squared Solstis) modulated by gated acousto-optic modulators (Gooch and Housego) that carve out short pulses with a rise time of 350 ns, and also shift the frequency of the laser (see Supporting Information Fig. S1). Pulses are detected using a single photon counting module (Excelitas Technologies Inc) with 400 ps temporal resolution.

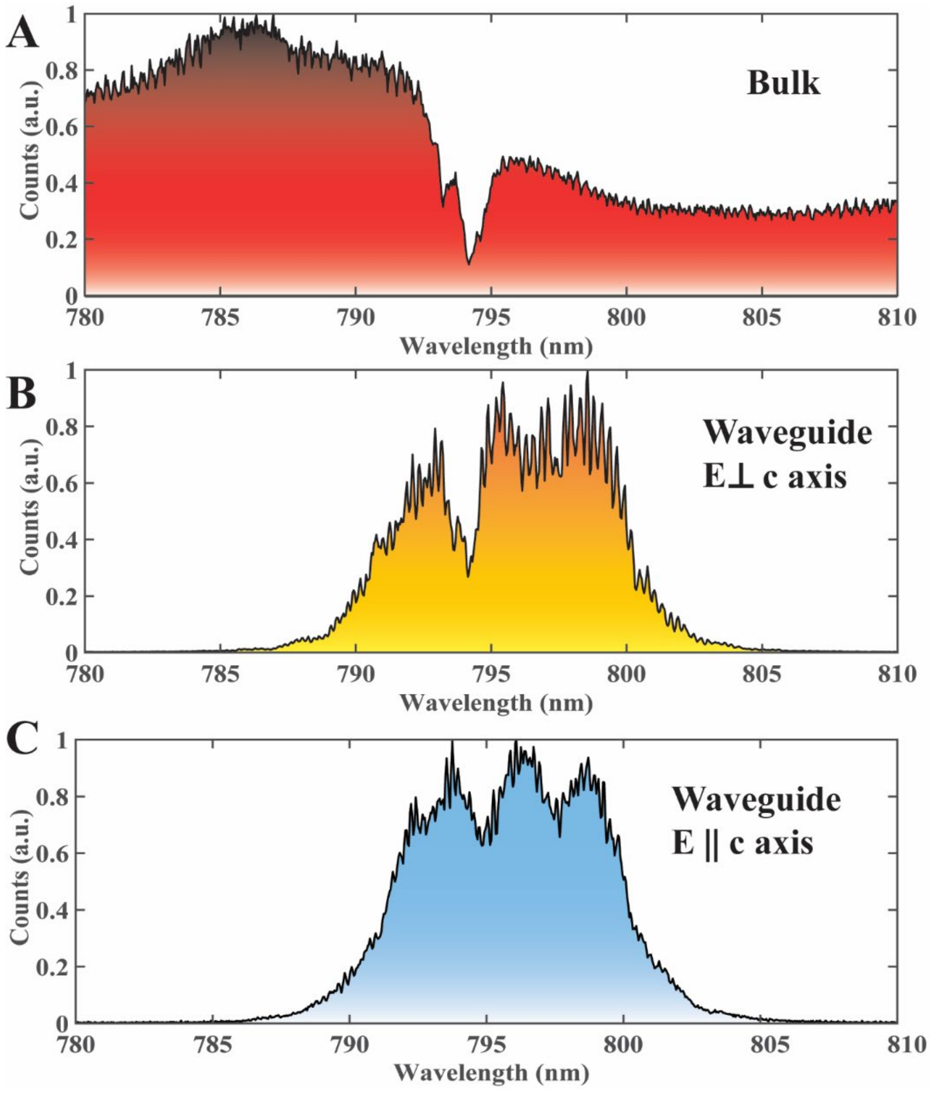

Figure 3.4.2. (A) Broadband transmission spectrum through a 1 mm length of Tm^{3+} doped bulk lithium niobate crystal with the electric field polarized perpendicular to the crystal *c* axis. (B)-(C) Broadband transmission spectrum filtered down to 10 nm, through a thin film waveguide with the electric field polarized perpendicular (B) and parallel (C) to the crystal *c* axis.

We first characterize the property of the bulk substrate (prior to smart-cut). To perform this measurement, we place the 500 μm-thick bulk substrate on top of a mirror and inject the beam from the top. We excite the sample with the supercontinuum laser and collect the reflected light. In this way the beam performs a double-pass through the bulk and therefore goes through 1 mm of material. Fig. 3.4.2(A) shows the spectrum collected through the bulk crystal with the electric field polarization perpendicular to the crystal *c* axis. The bulk crystal exhibits a strong absorption peak at the wavelength range of 794 nm due to Tm^{3+}, which is consistent with past measurements[64]. We observe a peak absorption of 75%, corresponding to an absorption coefficient of 14 cm^{-1} for the ions in the bulk crystal. This number is also consistent with past reported values for bulk Tm^{3+} in lithium niobate with similar doping densities[64]. The sharp absorption peak disappears (not shown) when we orient the polarization parallel to the *c* axis, as expected due to the local crystal symmetry of the lattice sites occupied by Tm^{3+} ions in lithium niobate.[64].

Next, we probe the thin film by performing waveguide absorption measurements. We excite one end of the waveguide at the grating with a supercontinuum source, filtered to 10 nm using a bandpass interference filter, and collect from the grating coupler at the other end. Fig. 3.4.2(B) shows the transmission spectrum through a 775 µm long waveguide with the electric field polarized perpendicular to the crystal axis. The waveguide transmission exhibits the same sharp absorption peak as the bulk at 794 nm. We observe a peak absorption of 66% in the waveguide. This corresponds to an absorption coefficient of 14 cm^{-1}, consistent with the bulk value. Fig. 3.4.2(C) shows the transmission spectrum through an orthogonal waveguide with the electric field polarized parallel to the crystal *c* axis. We observe a small dip corresponding to a 30% absorption. This is attributed to the 240 µm bending regions in the long racetrack shaped waveguides where the polarization rotates along the bends and overlaps with the direction perpendicular to the crystal *c* axis. (see Supporting Information Fig. S2) These measurements indicate that the optical absorption of the ions in the thin film is highly polarized, and that the Tm^{3+} ions retain the bulk absorption properties even after significant nanofabrication steps. The dips at 798 nm are due to the absorption with the electric field polarized parallel to the crystal axis, which has a different absorption resonance from the case when the electric field is polarized orthogonal to the crystal axis. In the bulk, we orient the electric field to be orthogonal to the crystal axis so there is no absorption at 798 nm. In the thin-film waveguide in Fig. 3.4.2b, we orient the waveguide so that the TE mode is orthogonal to the crystal axis. However, due to the bending regions of the racetrack shaped waveguides, (see Supporting information Fig. S2.) we observe some absorption at 798 nm. The absorption is even stronger when we orient the waveguide in the other direction so that the electric field is parallel to the crystal axis, as shown in Fig. 3.4.2c.

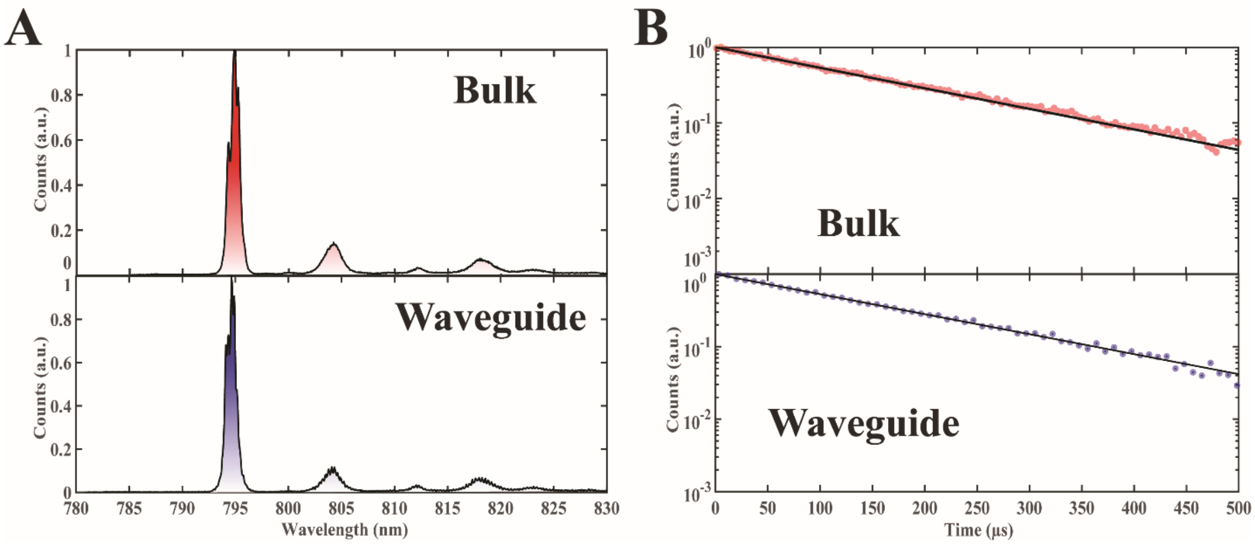

Figure 3.4.3. (A) Photoluminescence spectrum from bulk crystal and a waveguide in Tm^{3+} doped lithium niobate thin film. (B) Time resolved photoluminescence through a thin film waveguide and bulk crystal respectively. The solid black lines denote a fit to a single exponential decay. The fit reveals lifetimes of 157.4 ± 1.5 μs and 158 ± 2.8 μs in the thin film

and bulk respectively.

The inhomogeneous linewidth of the rare-earth ion ensemble is a good measure of the residual lattice strain in the host material. The spectral line shape reflects the local crystal field experienced by the ions. To further probe these properties, we perform photoluminescence spectroscopy of the ions in the bulk sample and the thin film waveguide. We use a narrow tunable laser (M Squared Solstis) to excite the fifth level of the $^3H_4$ excited state multiplet at 773.3925 nm. At 3.6 K the population relaxes to the lowest level of the excited state multiplet by phonon emission on a timescale much shorter than the fluorescence lifetime[64]. Fig 3.4.3(A) shows the photoluminescence spectra through the bulk sample and the thin film waveguides. Both spectra reveal similar line shapes for all the transitions from the lowest level of the excited state to the ground state multiplet. The bulk luminescence has a full width at half maximum of 0.7 ± 0.01 nm which is similar to the 0.69 ± 0.01 nm measured for the thin film waveguide. Furthermore, we do not observe appreciable background fluorescence[65] induced by the smart-cut process, which indicates that this process does not generate substantial fluorescence centers that can pollute the Tm^{3+} fluorescence.

In order to ascertain whether the smart-cut process introduces unwanted non-radiative decay, we perform time-resolved photoluminescence measurements. Additional non-radiative decay of in the thin film would lead to a shortened optical lifetime [25,59,66,67] or non-exponential luminescence decay[66]. We perform time-resolved photoluminescence on the ions in the thin film waveguides and the bulk using a modulated single frequency laser with a center frequency at 773.3925 nm. A gated acousto-optic modulator carves out the excitation laser into short pulses (see Supporting Information Fig. S1). Fig 3.4.3(B) shows the time resolved photoluminescence signal from a 15 μm long thin film waveguide and the bulk sample. Both the spectra are fit to a single exponential decay and reveal spontaneous emission lifetimes of 157.4 ± 1.5 μs and 158 ± 2.8 μs respectively, which are equivalent to within the sensitivity of the measurement. We therefore do not observe any additional source of non-radiative decay in the thin film material.

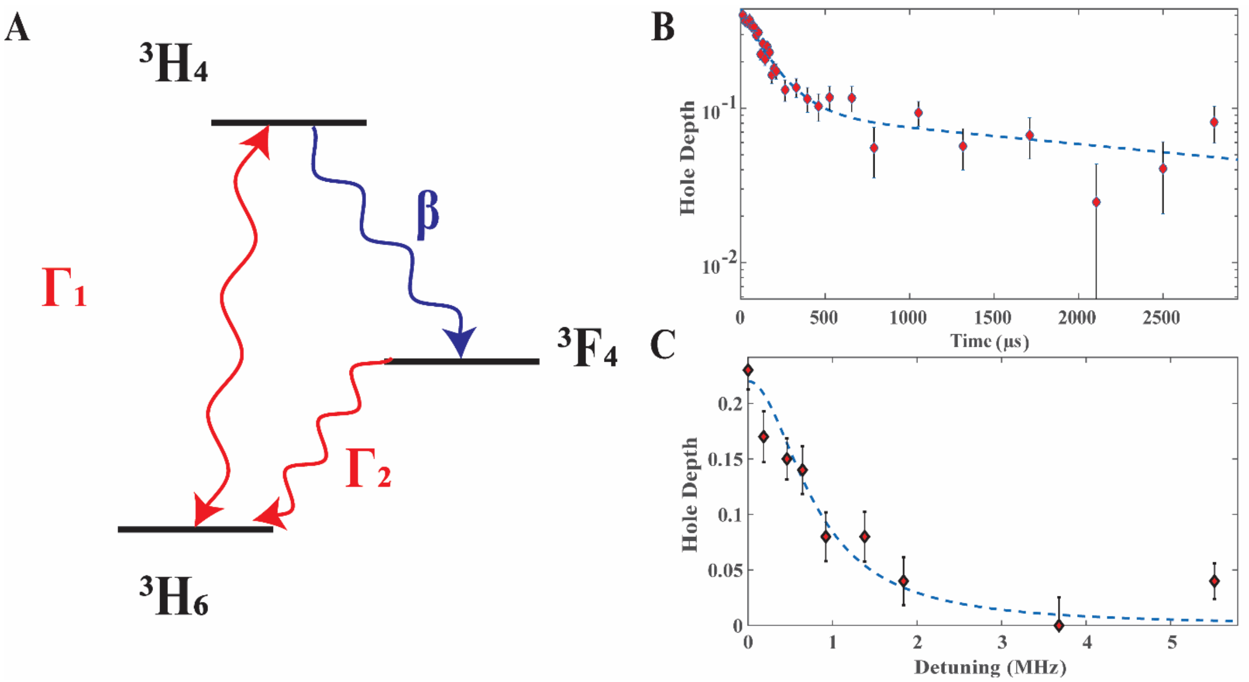

Figure 3.4.4. (A) Simplified energy level structure of Tm^{3+} ions in a lithium niobate thin film. Γ_1 and Γ_2 denote the decay rates from $^3H_4$ and $^3F_4$ to $^3H_6$ respectively. β denotes the branching ratio of the transition from $^3H_4$ to $^3F_4$. (B) Time resolved decay of a spectral hole in a thin film waveguide. The dashed line shows a fit to a biexponential decay. (C) Frequency resolved decay of a spectral hole in a thin film waveguide. The dashed line shows a fit to a Lorentzian profile.

One of the key features of a rare-earth ion ensemble is the ability to tailor the inhomogeneously broadened absorption profile by burning spectral holes. Spectral hole burning is a critical step for many applications in both classical and quantum optics[36]. A narrow spectral hole acts as a high quality factor frequency filter for optical signal processing [36,40], and also enables atomic frequency combs that are an essential step for ensemble optical quantum memory protocols [50,68]. Tm^{3+} ions in crystalline lithium niobate have a level structure as shown in Fig. 3.4.4(A) which allows for spectral hole burning[50,59,64,69]. Atoms excited to the $^3H_4$ state either decay back to the ground state $^3H_6$ level or to a metastable state $^3F_4$ via two dominant pathways. The shelving state has a long lifetime of several milliseconds. It acts as a population trap before finally decaying back to the ground state. This population trapping allows us to burn a spectral hole in Tm^{3+}.

To burn a spectral hole, we split the single frequency laser into two acousto-optic modulators to separately generate a burn pulse and a probe pulse (see Supporting Information Fig. S1). Varying time delays between the burn and the probe pulses maps out the decay of the spectral hole. Fig 3.4.4(B) plots the decay of a spectral hole burned at 794 nm in a waveguide patterned on the Tm^{3+} doped thin film. The plot follows a bi-exponential decay with lifetimes of 162 ± 16 μs (r_1) and 3 ± 1.6 ms (r_2) and a branching ratio (β) of 22 ± 6 % (see Supporting information on Branching Ratio Calculation). These lifetimes correspond to the spontaneous emission rate of the $^3H_4$ and the decay of the metastable $^3F_4$ respectively, while the branching ratio corresponds to the decay of the $^3H_4$ excited state to the metastable state. The values are consistent with previous measurements performed in bulk crystals[64]. These results suggest that ion sliced materials can be used for atomic frequency combs with similar performance to bulk structures, but in a compact integrated photonic form-factor.

The linewidth of the spectral holes puts a limit on the storage time of the optical quantum memories[19,34,36]. To measure this linewidth, we attenuate the laser burn power and burn a spectral hole to partial depth to limit power broadening. We scan the probe frequency with respect to the burn pulse, at a fixed time delay of 26 μs and map out the decay of the spectral hole. Fig. 3.4.4(C) shows the decay of the spectral hole when fit to a Lorentzian profile. The fit shows a linewidth of 1.6 ± 0.4 MHz. The inverse of the spectral hole linewidth puts a lower bound on the optical coherence time at 0.66 ± 0.16 μs. This value is already close to previous reports of a 1.6 μs coherence time of at 3.6 K,[59,64,69] measured using two pulse echo. The difference between these measurements may be due to power broadening, instantaneous spectral diffusion caused by the process of burning a hole, and by the laser linewidth. Further experiments using two pulse echo schemes would provide a more accurate measurement of the actual coherence time of the system. In our present experimental setup, we were only able to generate optical pulses of 700 ns due to the bandwidth limitations of the acousto-optic modulators and the spot size of the beam. These pulses are too long for a two-pulse echo measurement. By using faster AOMs and reducing the spot size we believe we can get optical pulses as short as 50 ns, which would be sufficient to perform an echo measurement.

One advantage of the thin film platform is that it enables waveguides with significantly smaller cross-sectional areas, which significantly reduces the power required to burn spectral holes. Our waveguides have a mode cross sectional area of only 0.07 μm^2 which is 500 times smaller than that of titanium in-diffused waveguides[59] in bulk lithium niobate. Thus, we expect to be able to burn spectral holes with much less power than that in bulk waveguides. To estimate the power in the waveguide mode we measure the end to end efficiency of the setup from the objective lens that focuses the light onto the input grating coupler, to the collection fiber that collects light from the output grating coupler. We measure this efficiency to be 10^{-6}. We assume that the efficiencies of the input and output grating coupler are the same, resulting in a coupling efficiency of about 10^{-3} for each coupler. Using this efficiency, we calculate that the peak power required to burn a hole to transparency in the waveguide using a 12.5 μs long laser pulse is only 10 nW. This is over two orders of magnitudes lower than previously reported values in bulk waveguides for the same length of the burn pulse[59]. We note that our grating coupler efficiency is low. There are several reasons for this. First, our waveguides are partially etched to 125 nm out of the 300 nm of thin lithium niobate, so the index contrast is lower than that used in previous work[70] where they etched almost completely through. Second, because we are working in a cryostat, our collection is performed 90 degrees out of plane. Creating efficient grating couplers that divert light vertically out of plane is challenging because the grating teeth have to be closely spaced and we are limited by the 45 degree angle sidewalls. Higher efficiency is possible if one allows the light to emit at a slight angle, but this geometry involves complicated the alignment of the objective lens and fiber collection. A deeper etch[70] or direct edge coupling[71,72] methods are potential methods to improve this efficiency.

In conclusion, we demonstrate an integrated photonic platform for rare-earth ions in a single crystal thin film which is compatible with scalable planar fabrication. Our technique preserves the desirable optical properties of the rare-earth ions in bulk crystal, paving the way for on-chip lasing, optical signal processing and quantum memory. Lithium niobate also has a strong piezo-electric coefficient that can tune and modulate the ion resonant frequencies to achieve controlled reversible inhomogeneous broadening of narrow absorption lines[59,68] Reducing the waveguide dimensions by going to a thin film substrate enables the creation of strong electric fields at lower voltages and higher bandwidths[73], which would significantly enhance the speed at which the ions can be tuned. Other rare-earth ion species such as Er^{3+} and Pr^{3+} can also be doped into the substrate to enable other wavelength ranges including the telecom band[51,60]. Patterning the substrate into nanophotonic cavities[62] could further enhance light-matter interactions, providing a pathway for spin-photon interfaces[74–76]. Ultimately, our results add tremendous functionality to the emerging field of lithium niobate integrated photonics by providing a compact and versatile optically active material that has broad applications in both classical and quantum optics.

Chapter 4: A Quantum Memory In Thin Film Lithium Niobate

4.1 Review

Quantum communication networks require methods to both transmit and store qubits, the building blocks of quantum information processing. Photons are the unique carriers of quantum information while atoms are currently the best quantum memories. Methods to store photons in an atomic systems therefore lie at the heart of long distance quantum communication[2]. The future quantum internet will therefore require compact photonic devices that can efficiently process and store photons.

Rare earth ion doped materials are an ideal atomic quantum memory for quantum communication. The materials possess electronic states that are naturally shielded from the environment higher level orbital states, making them insensitive to the crystal environment. Thus, rare-earth ions have extremely long optical and spin coherence times, making them an ideal quantum memory for quantum communication[42]. Furthermore, by leveraging techniques such as atomic frequency combs[77], they can store optical photons over long time periods with very high efficiency. They thus provide all of the necessary ingredients for advanced quantum networking protocols based on quantum repeaters[45]. But the majority of rare-earth ions are embedded in large bulk crystals. These materials cannot support compact integrated photonic waveguide and cavity structures, which are essential to develop compact and schedule quantum memories for large-scale deployment. Practical quantum devices must be compatible with wafer scale planar nanofabrication, which requires a thin-film material containing rare-earth ions deposited on top of a low index layer such as SiO_2. Such a material has not been available in the past.

We have developed such a material for the first time[78] exploiting the emerging commercial platform of thin film lithium niobate on insulator. Past work on bulk rare-earth ions doped in lithium niobate has already established these materials as an efficient optical quantum memory[50]. But all these methods used either bulk crystal or large ion diffused waveguides which require centimeter long devices and are therefore not suitable for compact integration. Extending these materials into a thin film platform combines the best of both worlds, a pristine quantum memory in a wafer structure that can support integrated photonic waveguides and cavities and is compatible with large-scale planar nanofabrication.

4.2 Integrated quantum memory in thin film lithium niobate

We demonstrate an integrated quantum memory with rare-earth ions in thin film lithium niobate. The ions in the thin film exhibit coherence times of 700 ns at 4K, similar to the ions in the bulk and experience no additional decoherence. Leveraging the strong optical confinement in the thin film waveguides, we demonstrate coherent rotations with Rabi frequencies over 1000X faster than that in ion diffused waveguides for the same drive power. Finally, we tailor the inhomogeneous absorption spectrum into a 100 MHz broad atomic frequency comb. We proceed to create optical delays on chip upto 250 ns by storing and retrieving photons in the atomic frequency comb. The new coherent light matter interface in thin film lithium niobate acts as a key enabler in an already rich optical platform representing a significant advancement in the field of integrated quantum photonics.

4.3 Device Structure and Fabrication

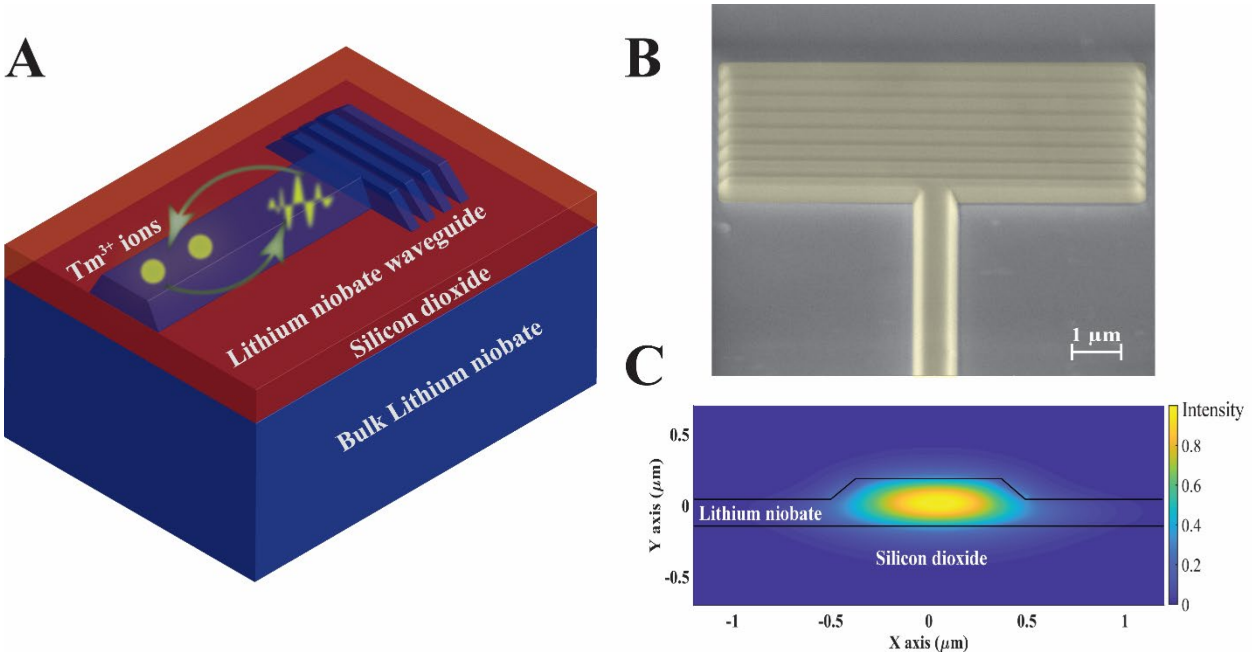

Figure 4.3.1. (A) Device geometry. Schematic of the cross-section of a waveguide etched in the heterogeneous material stack. (B) Scanning Electron Microscopy image of the waveguide with grating couplers patterned in the Tm^{3+} doped lithium niobate thin film. (C) Finite Difference Time Domain simulation showing the electric field distribution along the waveguide cross-section.

Fig 4.3.1(A) shows a schematic of the layer structure of the fabricated device. We begin with a bulk X-cut lithium niobate substrate doped with 0.1% Tm^{3+}. Using a commercial smart-cut process (NANOLN), we fabricate a 300 nm layer of doped single crystal lithium niobate wafer bonded to a 2 μm thick layer of silicon dioxide grown on undoped bulk lithium niobate as the substrate material. We etch waveguides into the doped thin film using a two-layer electron beam lithography and dry etching process. Fig. 4.3.1(B) shows a scanning electron microscope image of the fabricated waveguide along with grating couplers to couple light from the out of plane dimension. The waveguides have smooth sidewalls etched at an angle of 45 degrees. We select the waveguide geometry to be single mode at 794 nm which is the $^3H_6 \rightarrow {}^3H_4$ optical transition for the Tm^{3+} ions. Fig. 4.3.1(C) shows a finite difference time domain simulation of the electric field intensity inside the waveguides for the fundamental TE mode at this wavelength. The waveguides are 700 nm wide and constitute only a partial etch of the thin film with an etch depth of 125 nm. Such a design minimizes the interaction of the light with the etched sidewalls resulting in low propagation losses[61]. The optical mode exhibits transverse area of (176 nm X 400 nm) 0.07 μm^2, which is 3 orders of magnitude smaller than titanium in-diffused waveguides[59]. The mode is tightly confined in the thin lithium niobate film where it interacts with the Tm^{3+}. The direction of the waveguide must be selected carefully so that the TE mode of the waveguide aligns with the dipole moment of the ions, which are oriented perpendicular to the optical axis (*c* axis) of the lithium niobate substrate [50,59,64].

To pattern the thin film waveguide we first grow a 500 nm layer of amorphous silicon which acts as a hard mask. We spin a 300 nm layer of ZEP520A and pattern the samples using a 100 kV electron beam lithography system (Elionix). We deposit 10 nm chromium in an electron beam evaporator and perform metal liftoff to make a negative mask. Using chromium as a mask we first etch the silicon with a standard fluorine chemistry dry etching recipe. Now, with the silicon as a hard mask we transfer the pattern to the thin film lithium niobate using an optimized argon plasma physical etching technique. Finally, we use a 30% solution of KOH at 80° C to remove the remaining silicon. We grow a 2 μm layer of oxide on top of the waveguides to reduce scattering induced losses at the waveguide sidewalls.

4.3 Experimental Setup

To characterize the sample, we cool it down to 4 K in closed cycle cryostat (Attocube attoDRY). We use a confocal microscope with a diffraction limited spatial resolution between the excitation and the collection spots to perform transmission measurements through the thin film waveguides. To perform time-resolved measurements we use a single frequency laser (M Squared Solstis) modulated by gated acousto-optic modulators (Brimrose Corp.) that carve out short pulses with a rise time of 5 ns, and shift the frequency of the laser. Pulses are detected using a single photon counting module (Excelitas Technologies Inc) with 400 ps temporal resolution and a deadtime of about 70 ns.

4.4 Photon Echo Storage In An Inhomogeneously Broadened Medium

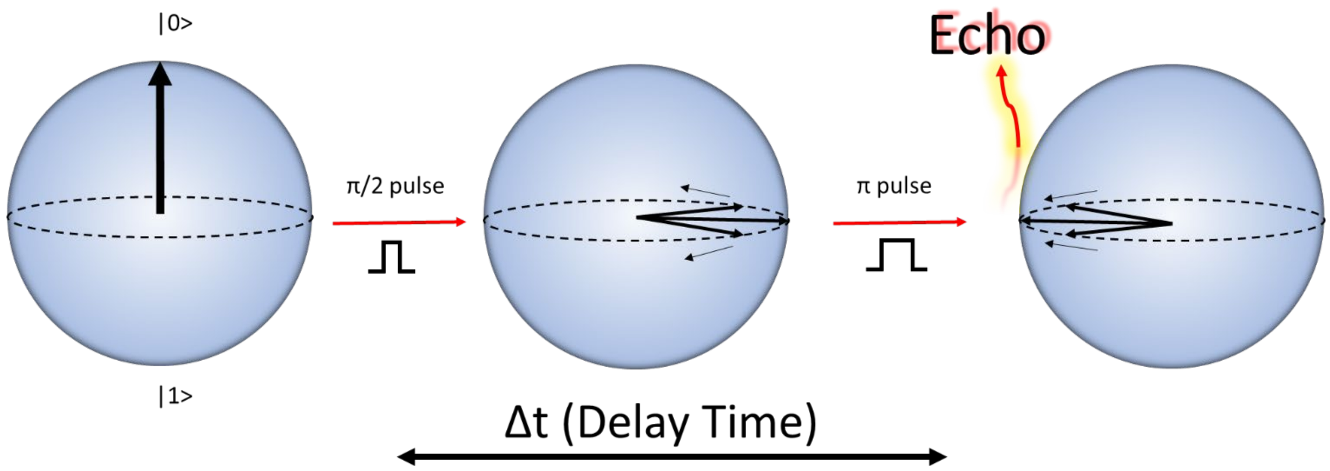

Figure 4.4.1 Schematic demonstrating photon echoes in an inhomogeneously broadened

medium.

The challenge of reversibly transferring quantum information between photons, i.e. moving carriers suitable for sending quantum information, and atoms, i.e. stationary carriers for storage, has triggered the development of quantum state storage protocols using photon echoes. It results from the observation that a pulse of light, absorbed in an inhomogeneously broadened medium with small homogeneous linewidth, can be forced to re-emerge from the medium sometime later as an echo. In an inhomogeneously broadened ensemble, the ensemble coherence dephases long before the individual dipoles stop oscillating. Photon echoes are an example of spontaneous recovery of the ensemble coherence that has been dephased after many relaxation times have elapsed. Recovery of the macroscopic polarization means recovery of the ability to emit radiation. The signature of a photon echo is the appearance of a burst of radiation from a long-quiescent sample of atoms. The burst occurs at a precisely predictable time, not randomly, and is due to a hidden long-term memory. It is possible to rephase the ensemble polarization, by getting all the Bloch vector components to realign using a rephasing pulse. This protocol is demonstrated in Fig. 4.4.1 where an input pulse first creates a superposition state which quickly dephases due to the large inhomogeneous broadening in the medium. A rephasing pulse is applied thereafter to realign the Bloch vectors and induce a photon echo. The first experimental demonstration of the so-called photon-echo has been observed independently by Kurnit[79] et al. 1964, respectively, as the optical analog to the well-known spin echo, discovered by Hahn[80] in 1950.

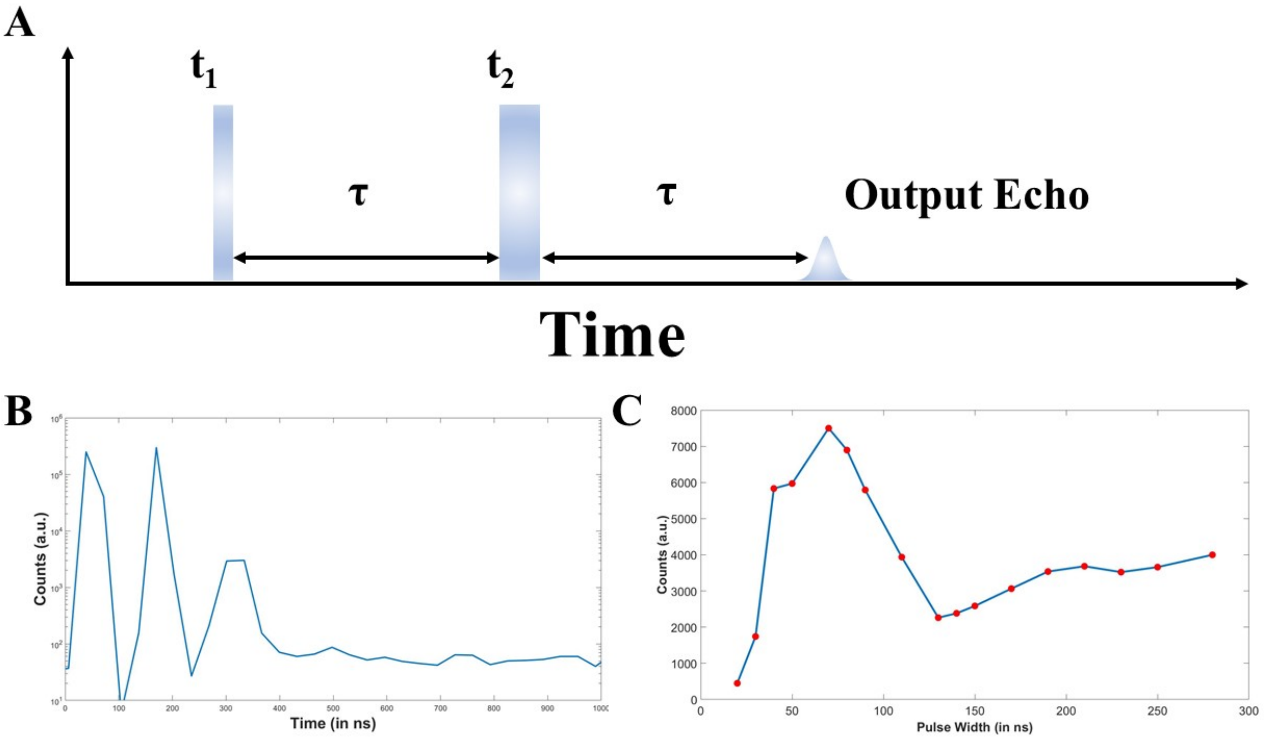

Figure 4.4.2. (A) Schematic showing the pulse sequence. (B) Time resolved experiment showing a photon echo. (C) Oscillation of echo intensity with increasing width of the rephasing pulse. The periodic signal reveals the ensemble averaged Rabi frequency of the coupled ions.

The photon-echo pulse sequence is outlined in Figure 4.4.2(A). The ensemble is driven into a superposition state by a pulse of width t_1. After a very short time has passed the inhomogeneously broadened ensemble polarization will dephase, and the radiation ceases. Time τ later, a rephasing pulse of width t_2 is applied. This inverts the y-component of the Bloch vector and the dipoles begin to refocus. After further time τ has passed, the Bloch vectors are all aligned once again, and the ensemble radiates. This revived free induction decay is an echo of the initial ensemble coherence. The photon echo intensity is maximum when the pulse area of the rephasing pulse represents an odd multiple of the π pulse. It is minimum when the corresponding pulse area is an even multiple of the π pulse. Thus, by varying the width, t_2 of the rephasing pulse, we trace out the peaks and valleys of the emitted photon echo intensity. The minimum pulse width, t_2 that results in the first peak provides the frequency of coherent oscillations of the dipole transition for the given driving strength.

To perform the photon echo experiments, we use an acoustic optic modulator with a modulation frequency of 400 MHz (Brimrose Corp.) to gate a single frequency M2 Solistis laser emitting at a resonant frequency of 794.25 nm, which is at the center of the inhomogeneous linewidth of the ion absorption. We use an arbitrary waveform generator (Tektronix) to control the modulator and carve out the desired pulse sequence. We detect the signal using a single photon counting module (Excelitas).

Figure 4.4.2(B) denotes the time resolved signal of a similar photon echo experiment with a 35 ns input pulse and 70ns rephasing pulse separated by 160ns. The Bloch vectors rephase and emit a bright echo 160ns after the rephasing pulse. In order to optimize the driving strength of the rephasing pulse, we keep the width t_1 of the first pulse fixed at 35 ns and sweep the width, t_2 of the rephasing pulse from a minimum of 20 ns to a maximum of 280 ns keeping gap between the centers of the two pulses fixed at 400 ns. Figure 4.4.2(C) plots the output echo intensity as the rephasing pulse width increases. We observe an oscillatory behaviour with a maxima when the rephasing pulse is a π pulse and a minima when the rephasing pulse is 2π. The oscillation contrast dies out after 3π due to dephasing in the system. From the width of the π pulse we extract the driving frequency of the dipole transition as 44.9 MHz (π/t_2) for a driving power of 1 μW in the waveguide. The power inside the thin film waveguide is 1000X lower than the power inside an ion-diffused waveguide to achieve the same driving frequency. This is a consequence of the extreme light matter confinement in the thin film waveguide producing a mode cross-section which 1000X smaller than that in the previous ion-diffused devices[25].

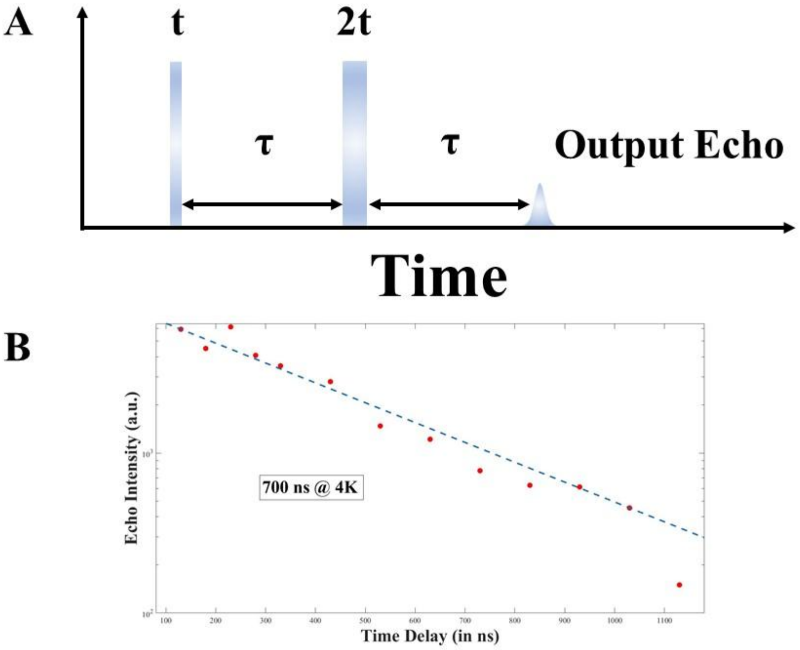

Figure 4.4.3 (A) Schematic showing the pulse sequence for two photon echo decays. (B) Experiment showing the decay of photon echoes with increasing storage time.

The maximum storage time in the system is fundamentally limited by the rate of decoherence that the ion ensemble experiences. An input pulse imprinted onto the broad ensemble of atomic dipoles, starts to dephase. The rate of change of phase of the different frequencies has a constant component as well as a time variable component. This time variable component is present because each ion in the ensemble experiences a different dynamic environment in the crystal that imparts arbitrary additional phases. This dynamic component cannot be realigned by a single rephasing π pulse. Hence, for increasing storage times the arbitrary time varying phases start to dominate. Thus, we see that the echo intensity decreases exponentially with longer storage times. This characteristic decay time or the coherence time, is a function of the ion species and the crystal environment. The coherence time thus puts a fundamental limit on the maximum storage time for quantum information in an ion ensemble.

In order to measure the coherence time of thulium ions in thin film lithium niobate, we set the width, t_1 to $\pi/2$, t_2 to π and sweep the delay, τ between the two pulses and observe the rate of decay of the output echo intensity. Such a pulse sequence is shown in Figure 4.4.3(A). We plot out the echo intensity with increasing delay times and observe an exponential decay with a time constant of 350 ns. Thus, the characteristic coherence time, T_2 (2τ) is 700ns at 4K. From this, we extract the homogeneous linewidth of thulium ions in thin film lithium niobate at 4K as ($1/\pi T_2$) 450 KHz. This is comparable to previous measurements for thulium ions in bulk lithium niobate at 4K[64]. This reiterates the assertion that the ions in the thin film maintain the same optical and coherence qualities as the ions in bulk devices[81].

4.5 Atomic Frequency Comb Quantum Memory

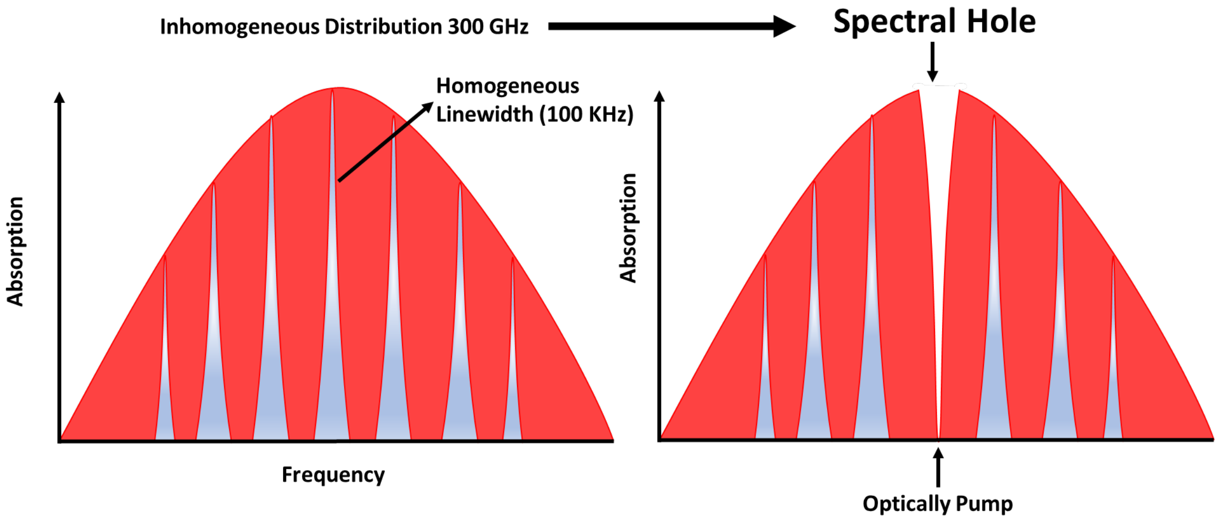

Figure 4.5.1 Schematic showing spectral tailoring in an inhomogeneously broadened ensemble of thulium ions in thin film lithium niobate.

Thulium ions in thin film lithium niobate provide a large inhomogeneous profile of 300 GHz. However, each ion has a narrow homogeneous linewidth of 450 KHz at 4K. This is demonstrated in the schematic in Figure 4.5.1. Now, if we come in with a narrow frequency laser and optically pump an ion, we can burn a spectral hole. In this way we can tailor the inhomogeneous absorption profile of the ion ensemble and implement the desired quantum storage protocol.

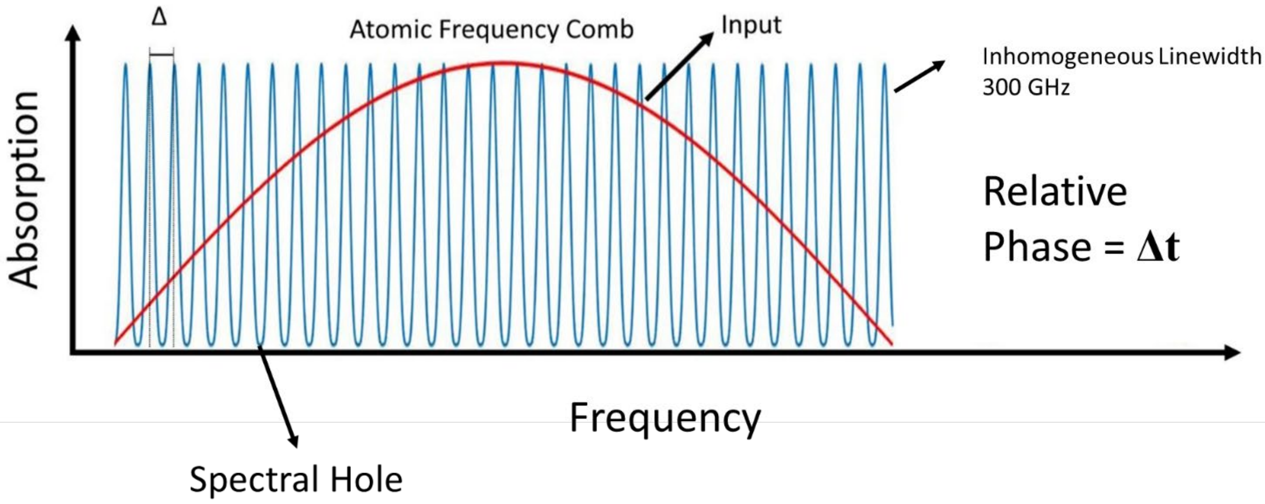

Figure 4.5.2 Schematic showing an atomic frequency comb imprinted on the inhomogeneous thulium ion ensemble.

We implement the atomic frequency comb protocol to achieve a quantum memory in the inhomogeneous ensemble of thulium ions in thin film lithium niobate. We use a narrow frequency laser and burn spectral holes at a periodic frequency interval, Δ. In this way we tailor the population of the atoms in the ensemble and imprint an atomic frequency comb. Now, we can store an input pulse which is broad in the frequency domain with respect to the width of the comb teeth. The different frequencies in the input are absorbed by the different teeth of the atomic frequency comb. As time evolves, the different dipoles pick up a relative phase of Δt. Now, after a time, 2π/Δ all the dipoles in the ensemble rephase and emit an output echo. Figure 4.5.2 demonstrates the schematic for the atomic frequency comb storage protocol. In this way we implement fixed time, broadband storage in the thulium ion ensemble.

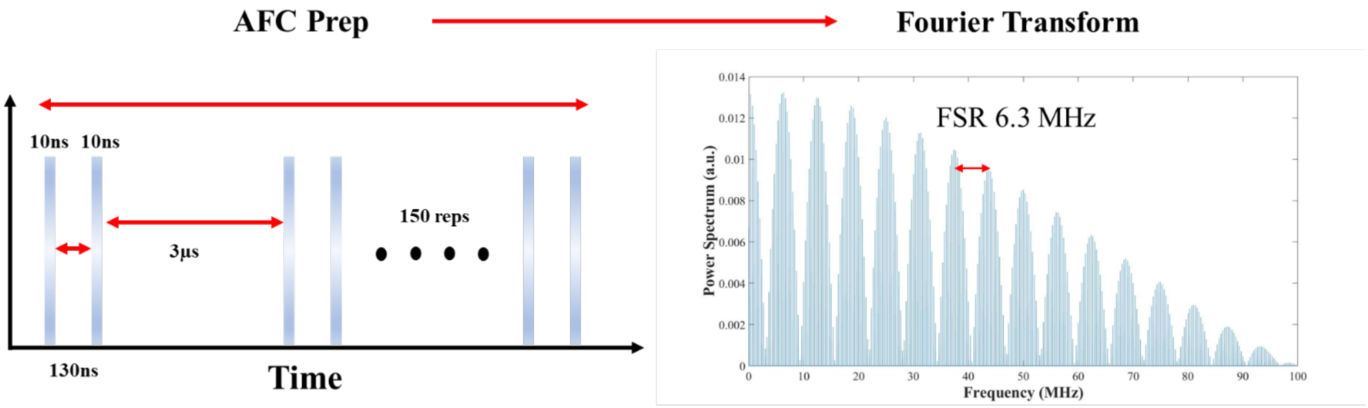

Figure 4.5.3 Schematic demonstrating the atomic frequency comb preparation sequence in the time as well as the frequency domain.

In order to prepare an atomic frequency comb, we carve out a periodic sequency of two 10 ns pulses, separated by the storage time, 150 ns and repeat the pulses with a period of 3 μs, which is long compared to the sample coherence time. We send a series of 150 pulses to the sample. The time domain implementation as well as the corresponding Fourier spectrum of such a pulse sequence is shown in Figure 4.5.3. We see that in the frequency domain this pulse sequence represents a frequency comb with a teeth separation of 6.3 MHz. We use a weak chirped probe pulse with a bandwidth of 50 MHz, to scan the atomic frequency comb structure that is imprinted on the ion ensemble.

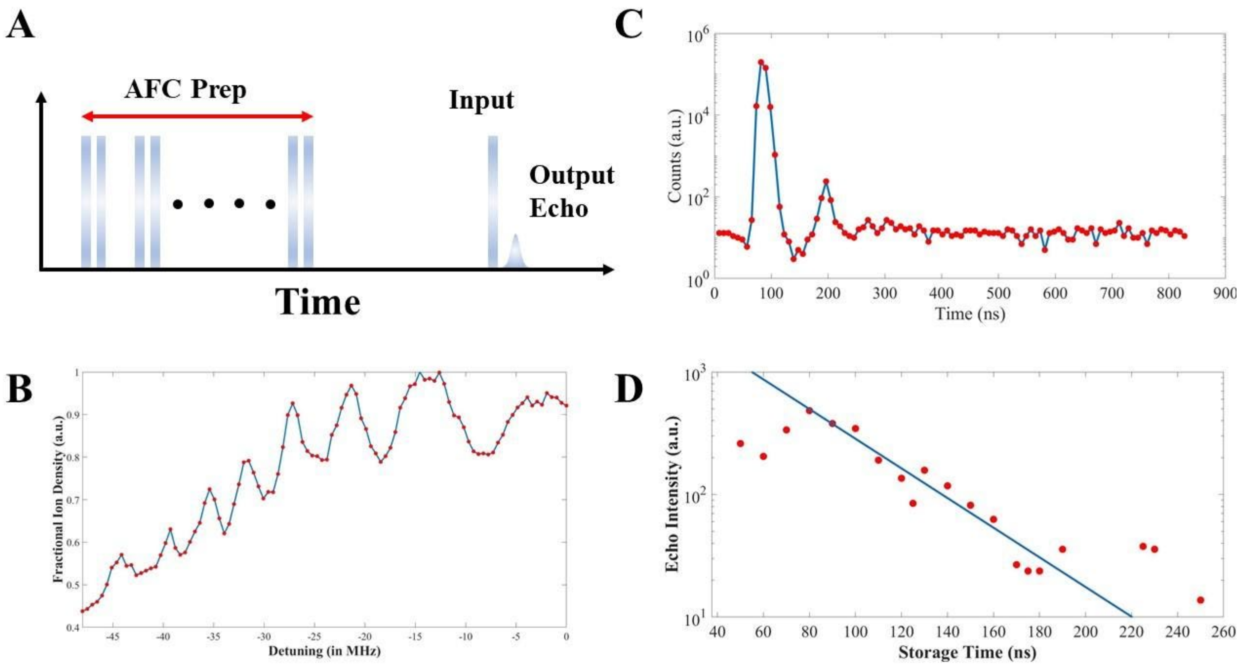

Figure 4.5.4 (A) Schematic showing the experimental pulse sequence. (B) Broadband frequency sweep showing the structure of the atomic frequency comb. (C) Experiment showing photon storage and retrieval in the atomic frequency comb memory. (D) Experiment showing the decay of echo intensity for increasing storage time.

Figure 4.5.4(A) demonstrates the pulse sequence for atomic frequency comb storage in the thulium ion ensemble. At first, we implement the pulse sequence for preparing an atomic frequency comb, then we wait for the spontaneous emission background to decay and finally we shine a single 10 ns input pulse, with a bandwidth equal to that of the entire comb. We can tune the storage time by sweeping the delay between the two pulses in the comb preparation sequence.

Figure 4.5.4(B) shows the snapshot of the atomic frequency comb imprinted on the thulium ion ensemble. The envelope of the curve is the shape of the chirped probe pulse that is used to scan the comb. This envelope is modulated by the comb structure imprinted on the ions ensemble absorption. We observe that the atomic frequency comb has an average free spectral range of 6.3 MHz by using the first five teeth of the comb. The optical depth of the comb teeth is about 0.23 and the FWHM is about 3.2 MHz. Thus, the finesse of the comb, defined as the ratio of the free spectral range and the teeth width is about 2.

Figure 4.5.4(C) demonstrates an example of light storage in the atomic frequency comb with a storage time of 100 ns. We store a bandwidth matched input pulse of width 10 ns and observe a bright echo after 100 ns. We prepare a variety of atomic frequency combs by sweeping the storage time parameter and we observe an exponential decay in the storage echo intensity for increasing storage time. We observe that we are able to store and retrieve light on chip upto an optical delay of 250 ns with an output SNR or 3.

In conclusion, we demonstrate an atomic frequency comb quantum memory in thin film lithium niobate with a thulium ion ensemble. We use optically pump population into the shelving state to burn spectral holes and pattern the inhomogeneous ensemble into an atomic frequency comb. We can further improve the optical depth of the atomic frequency comb by burning spectral holes in the presence of a magnetic field and using the Zeeman split levels to pattern the absorption spectrum[59]. This is the first demonstration of an atomic frequency comb in a monolithic thin film device. Such an implementation paves way for scalable quantum photonic systems where one can store and manipulate light on chip with high bandwidth and low powers.

Chapter 5: Conclusion And Outlook

5.1 Mimicking Infinite Length On Chip

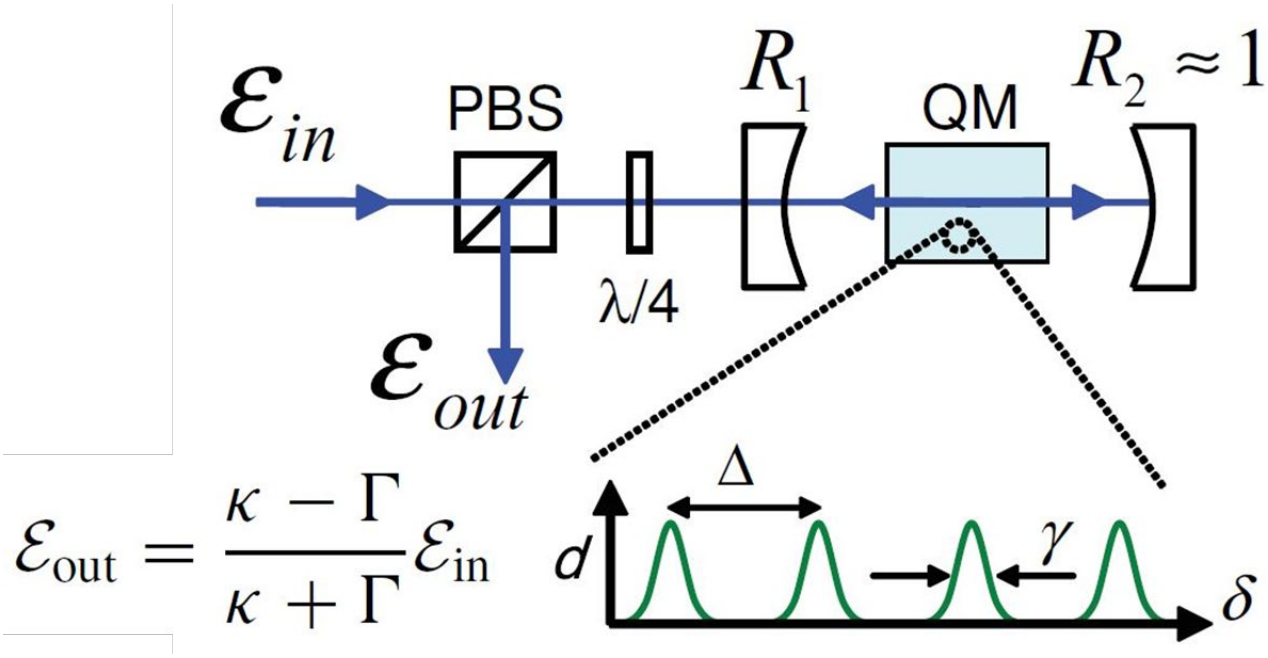

Figure 5.1.1 Atomic frequency comb quantum memory in an impedance matched cavity.

The efficiency of such quantum memories is limited by the optical depth of the absorber. Optical absorption follows an exponential decay. We would need an infinite length of waveguide to theoretically produce perfect absorption. However, we can use an impedance matched cavity to mimick infinite length. Such a cavity is one where the cavity mirror loss, κ equals the round trip absorption loss, Γ. An incident input pulse, ε_{in} on such a cavity is partially reflected from the first mirror. This reflection interferes with the cavity output and is quenched, ε_{out} for the impedance matching condition, $\kappa = \Gamma$. In such a situation, an incident pulse, ε_{in} is completely absorbed inside the cavity. The comb efficiency is only limited in by the intrinsic limit of the comb finesse, Δ/γ, where Δ denotes the comb free spectral range and γ denotes the FWHM of the comb teeth.

5.2 A Pathway to On-Demand Retrieval

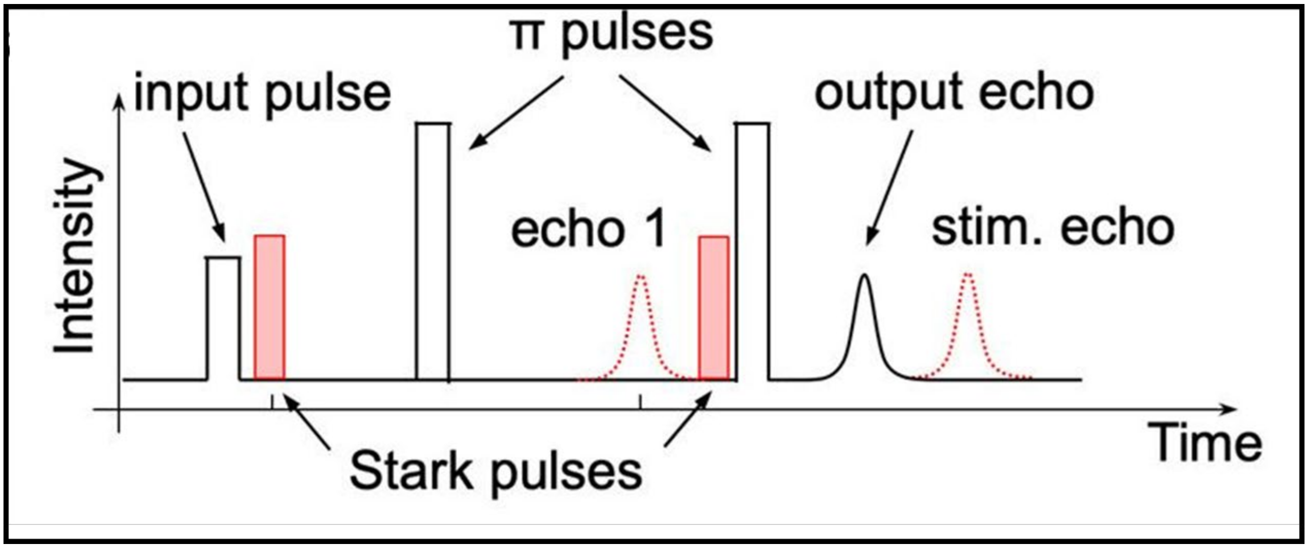

Figure 5.2.1 On-demand storage and retrieval in rare earth doped nanoparticle quantum memory.

In a recent demonstration[82], authors have successfully used Stark shifts to retrieve the photon echo on demand. Such a demonstration is shown in Figure 5.2.1. A π/2 Stark pulse is applied to the rare earth ion ensemble after the input pulse. Half of the rare earth dipoles align parallel with the pulse and half of them are aligned anti-parallel. Thus, the Stark shifted dipole ensemble gains an additional relative phase of π that quenches any echo emission after the rephasing pulse. Consequently, a π/2 Stark pulse with the reverse polarity wipes out the phase on the ensemble and we can retrieve the echo with another rephasing pulse. Such a protocol allows for on-demand retrieval in a photon echo quantum memory. Thin film lithium niobate allows for waveguides with a tiny form factor and compact electrodes. This would result in low voltage Stark pulses and a small form factor quantum memory with on-demand retrieval.

5.3 An Integrated Quantum Memory with On-Demand Retrieval

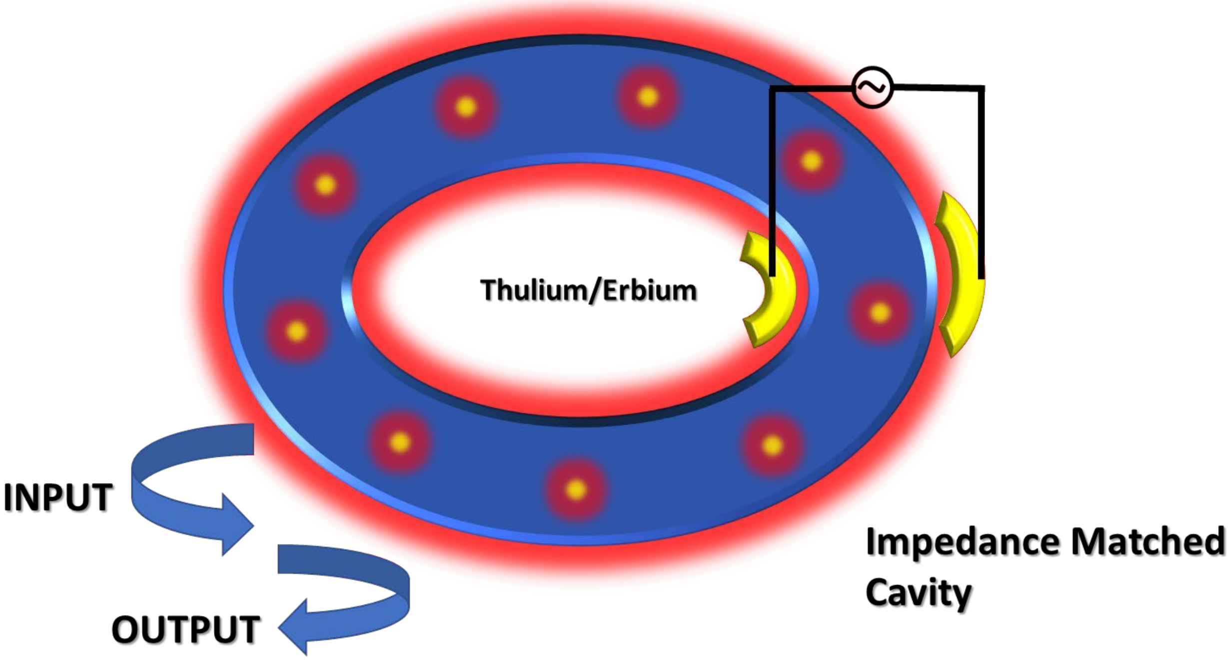

Figure 5.3.1 Schematic showing an integrated quantum memory with high efficiency and on-demand retrieval.

We propose as future work, an impedance matched cavity in thin film lithium niobate doped with rare earth ions, Thulium/Erbium absorbing at the NIR or telecom respectively. These ion species have a narrow homogeneous linewidth and a large inhomogeneous broadening of several 100 GHz to work with. Hence, they are perfect for broadband photon echo quantum memory. An impedance matched cavity allows the input signal to be completely absorbed within the cavity resulting in an optimal storage efficiency. Integrated electrodes with the thin film lithium niobate platform are already shown to be very efficient[73]. These can be used to implement Stark pulses and achieve an on-demand, high efficiency quantum memory all with a small form factor on chip.

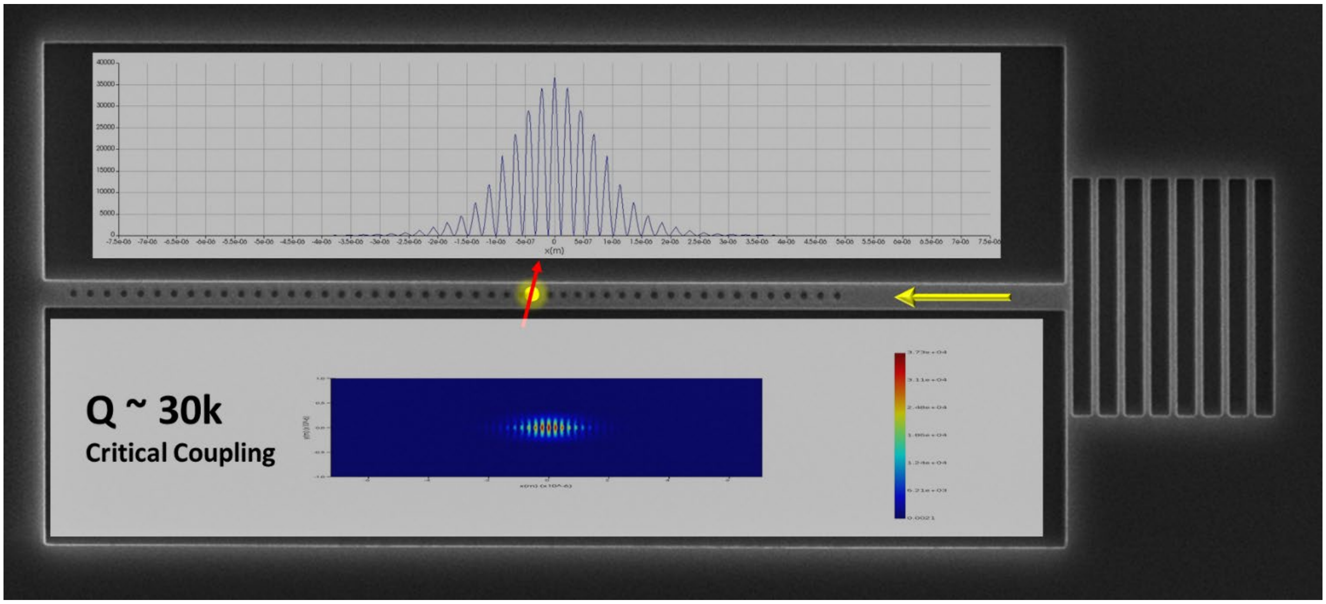

Figure 5.3.2 SEM image of a photonic crystal nanobeam cavity in thulium doped thin film lithium niobate.

In recent times we are running a collaborative effort with Prof. Qiang Lin at Rochester to make nanobeam photonic crystal cavities in thulium doped thin film lithium niobate. Fig. 5.4 an SEM image of the mask for etching one such cavity. The single sided cavity is designed in Lumerical to achieve a quality factor of 30000, which would be limited by our expected scattering losses in the cavity. We use grating couplers to couple light in and out of the single sided cavity. The rare earth ion ensemble at the cavity maxima experiences a very high optical density of states and we expect to see significantly higher light matter coupling compared to the waveguides. This would allow for extremely low power control and spectral tailoring of the ions as well as a highly efficient, scalable quantum memory.

Appendix 1: A Fast Integrated Single Photon Source

1.1 SEM Images with Monolayer Coverage

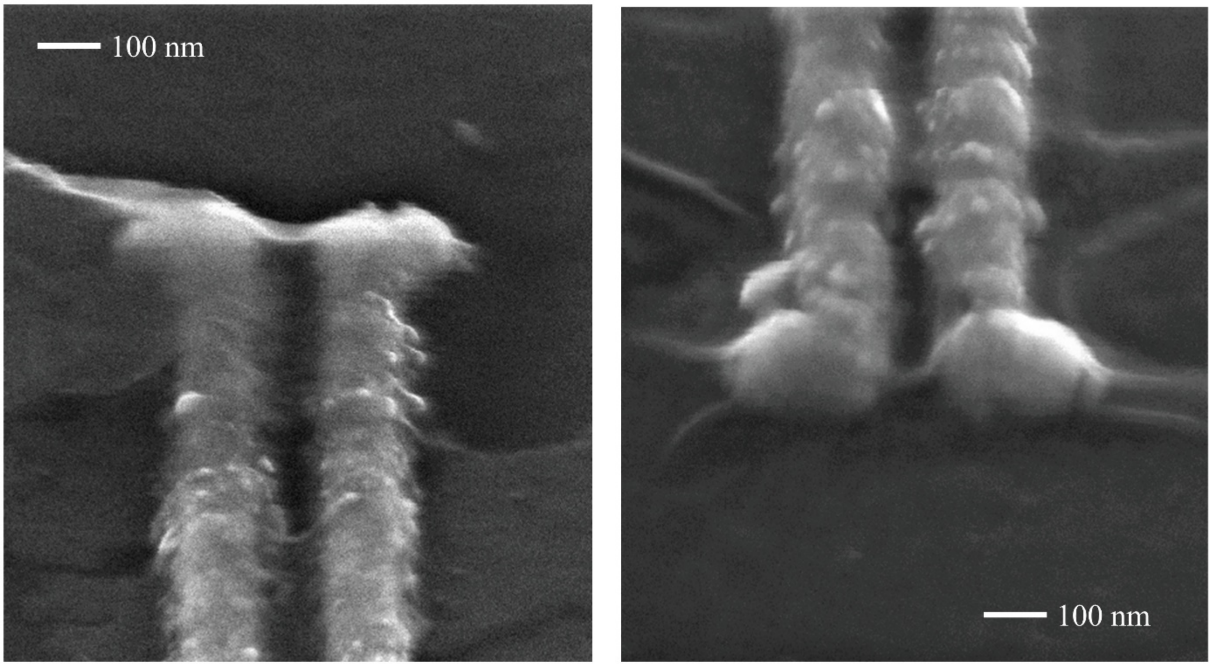

Fig. A1.1 SEM images taken at a 55° tilt angle showing how the monolayer bends across the gap in the MIM waveguides.

1.2 Atomic Force Microscopy Images

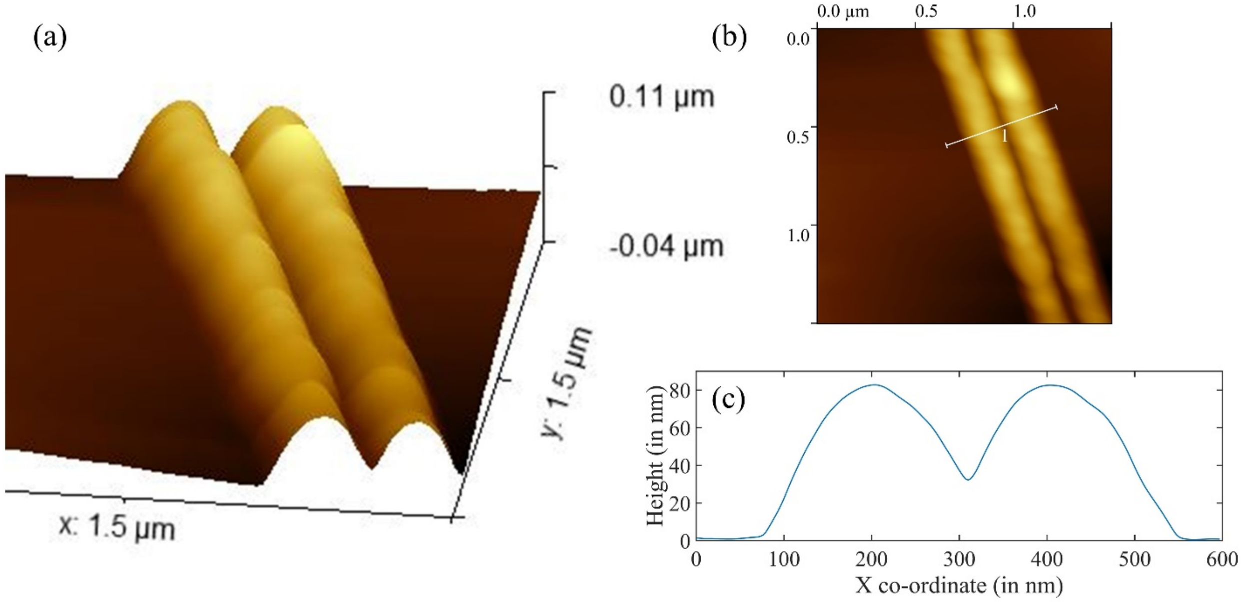

Fig A1.2 (a) 3D color map showing a perspective view of an atomic force microscopy image of a MIM waveguide. (b) 2D color map showing an atomic force microscopy image of a MIM waveguide. (c) Atomic force microscopy profile of the MIM waveguide across the line cut shown in (b).

1.3 Cross Polarized Doublet

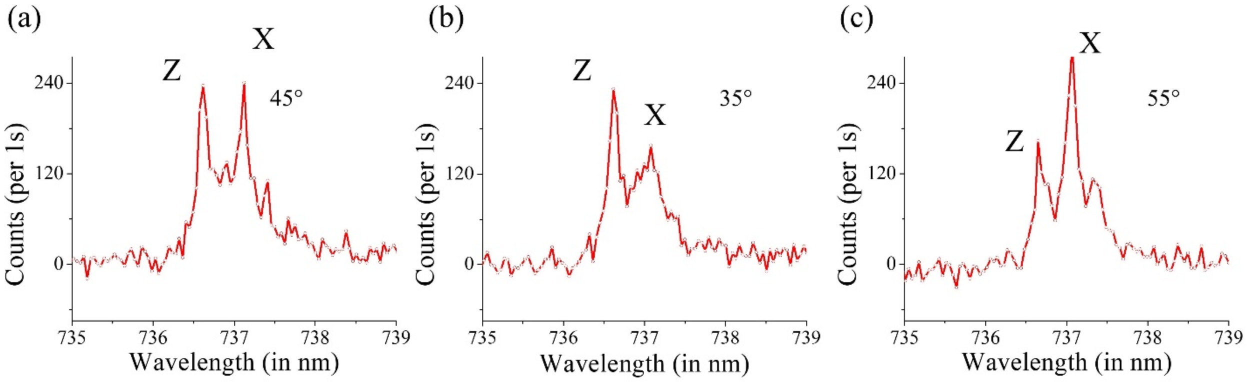

Fig. A1.3. Polarization resolved spectra of the defect at the location A marked in Fig 3(a) with the excitation and the collection aligned at the same point, A. (a) Spectrum when the collection polarization is aligned half-way between the orthogonally polarized doublet. (b) Spectrum when the collection polarization is rotated 10° clockwise from the position in (a). (c) Spectrum when the collection polarization is rotated 10° anticlockwise from the position in (a).

1.4 Addressing the issue of pump coupling

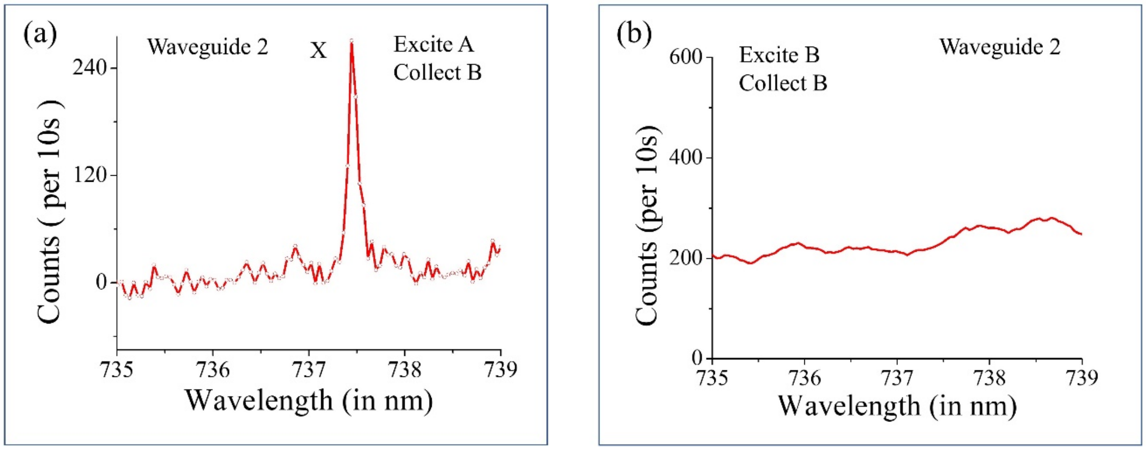

Fig. A1.4. (a) Photoluminescence spectrum when we excite Waveguide 2 at A and collect at B. (b) Photoluminescence spectrum when we excite Waveguide 2 at B and collect at B.

In Fig A1.4 (a) we excite at the location, A of the defect peak and we can see a sharp quantum dot like peak, X corresponding to the defect peak when we collect the scattered signal at B. If this signal were due to the pump coupling to the waveguide and exciting a different defect, we would expect to see the same feature when we move the excitation spot to the other end, B of the waveguide, keeping the collection spot the same (B). However, contrary to this we do not observe any quantum dot like emission feature but simply the background photoluminescence of the ensemble of defects of the monolayer as shown in Fig A1.4 (b). This leads us to believe that the pump does not efficiently couple to the waveguide. Hence, with the collection spot centered at B, we can see the peak X only when we keep the excitation spot at the location, A of the defect.

Appendix 2: Rare Earth Doped Thin Film Lithium Niobate

2.1 Experimental Setup

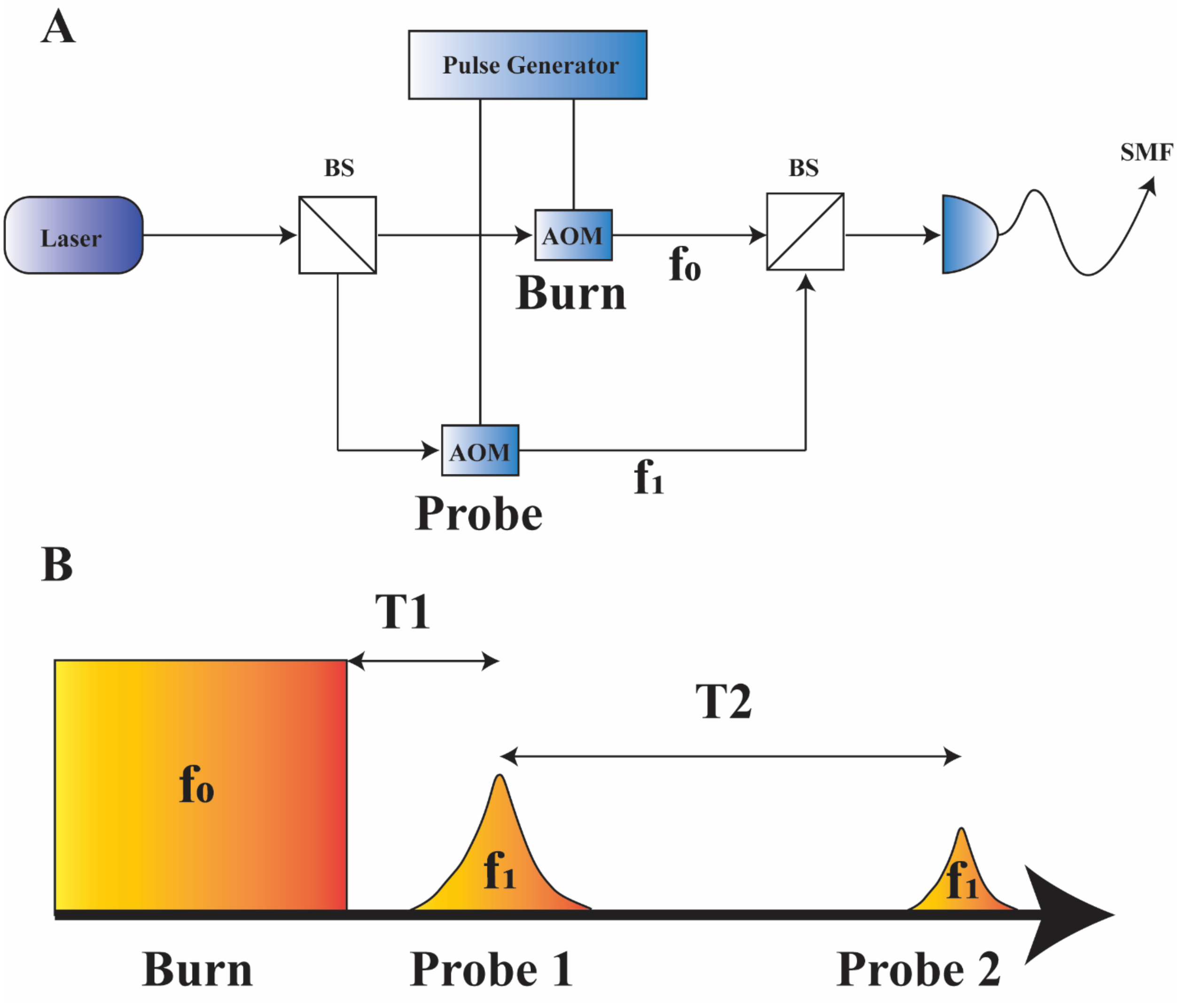

Figure A2.1. (A) Schematic of the setup for generating optical pulses. Laser, Single Frequency

MSquared Solistis; BS, Beam Splitter; AOM, Acousto-optic modulator; SMF, Single Mode Fiber; f_0, Burn frequency; f_1, Probe frequency. (B) Pulse sequence for time and frequency resolved spectral hole burning. T1 denotes the delay between the Burn and Probe1. T2 denotes the delay between Probe1 and Probe2.

2.2 Time Resolved Photoluminescence Experiments

For time resolved photoluminescence we carve out 500 ms long pulses using one of the AOMs, at 773.3925 nm to excite the fifth level of the $^3H_4$ excited state multiplet in the Tm^{3+} ions. We record the time resolved decay of the photoluminescence signal on a single photon counting module (Excelitas Technologies Inc), spectrally filtered down to a width of 0.1 nm using a spectrometer (Princeton instruments) as a filter.

2.3 Spectral Hole Burning Experiments

To perform spectral hole burning measurements we use two AOMs to carve out pulses at two independent frequencies, f_0 and f_1, from the single frequency input laser. We can switch the AOMs by means of an RF switch (Mini circuits) and control pulses generated by an arbitrary function generator (Tektronix). We drive the AOMs using a pair of Voltage Controlled Oscillators (Mini circuits) which can be tuned to independently control the output frequencies f_0 and f_1.

1) For time resolved spectral hole burning experiments, we use a 12.5 μs long burn pulse with a pulse power of 30 μW before the objective lens, at a frequency f_0. We generate a probe with a pulse power of about 0.3 μW before the objective lens. We tune the

frequencies of the burn and the probe pulses on resonances by interfering them on a fast photodetector (Thorlabs) and minimizing the observed beat frequency. To perform the experiment, we use a long delay, T2 of about 5 ms between two probe pulses vary the delay T1. The difference in the integrated area between the two probes represents the depth of a spectral hole at a time, T1.

2) For frequency resolved spectral hole burning experiments, we attenuate the burn pulse to about 3 μW before the objective lens. Keeping T1 and T2 fixed we sweep the frequency, f_1 of the of the probe with respect to the frequency f_0 of the burn pulse and map out the difference in the integrated areas between the two probe pulses which represents the hole depth.

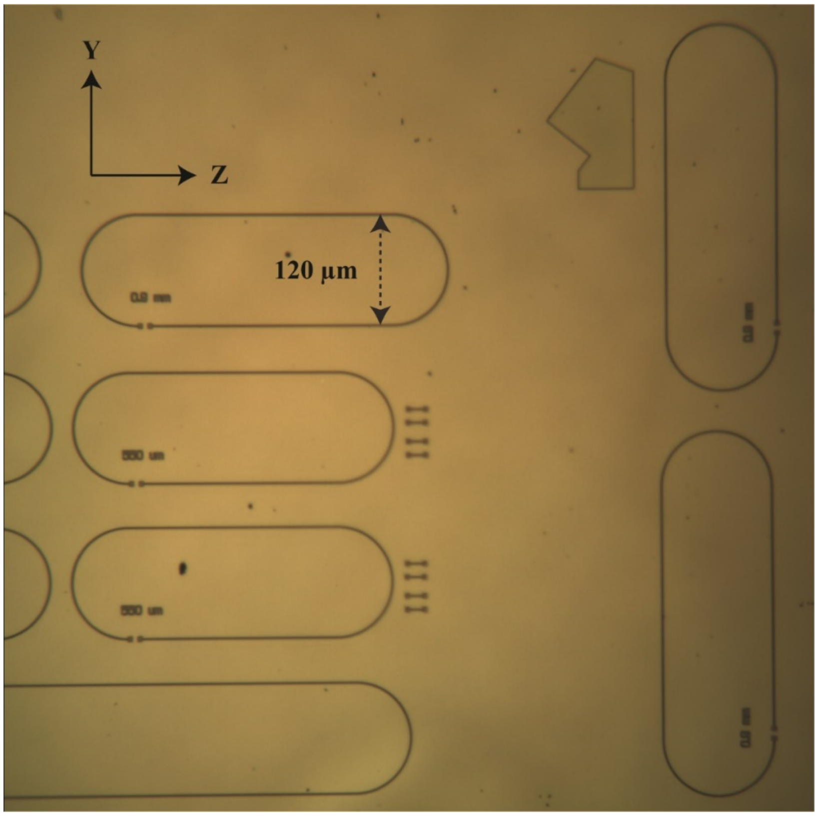

Figure A2.2 Optical microscope image of a representative sample. The crystal *c* axis is oriented along the Z direction. Racetrack shaped waveguides are fabricated orthogonally with respect to the *c* axis of the crystal.

2.4 Waveguide Absorption Experiments

Figure S2 shows a widefield optical microscope image of racetrack shaped waveguides fabricated in thin film lithium niobate oriented orthogonal and parallel to the crystal axis. Our measurement microscope has a 40 µm wide field of view. To accommodate both the excitation and the collection within the same field of view we fabricate long racetrack shaped waveguides that wrap around. As a result, the polarization of light rotates along the bends and overlaps with the orthogonal direction.

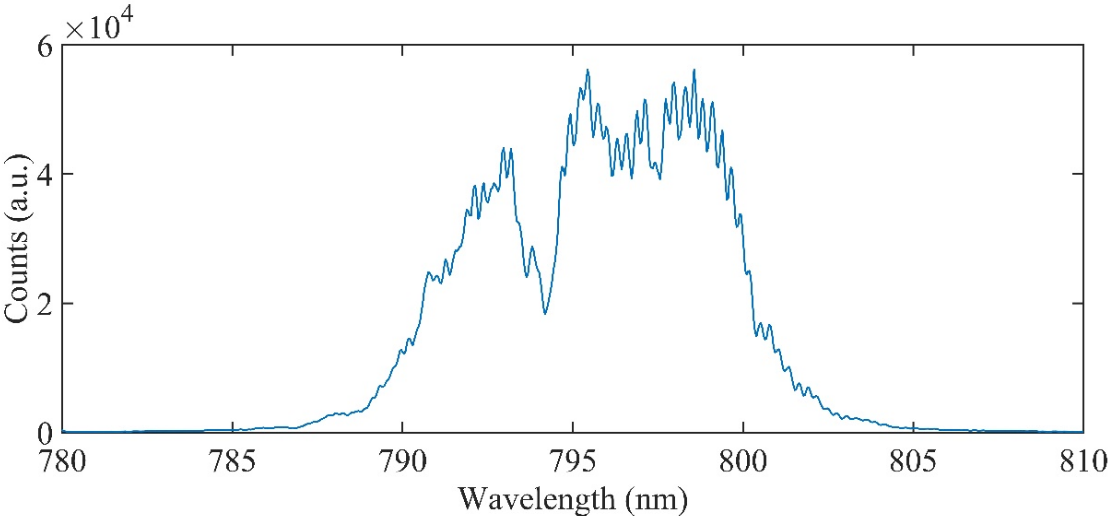

Figure A2.4 Shows the result of a digital 4 point moving average filter on Fig. 3.4.2(B) in the main manuscript.

The thin film waveguides suffer from high frequency Fabry-Perot oscillations. A low pass filter on the absorption spectrum shows close agreement between the bulk and the thin film absorption measurements in Fig. 3.4.2 (A) and Fig. 3.4.2 (B) respectively. However, such a filtering has the effect of changing the linewidth of the transition. Fig. A2.4 shows the result of digital low pass filtering (4 point moving average) of Fig. 3.4.2 (B).

2.5 Branching Ratio Calculation

To measure the branching ratio, we fit the time resolved decay of the spectral hole in Fig. 4b to the following biexponential:

$$Hole\ depth = (a-b)*exp(-t/t1) + b*exp(-t/t2);$$

$t1$ and $t2$ are the two decay constants corresponding to the spontaneous emission rate of the $^3H_4$ and the decay of the metastable $^3F_4$ respectively. The branching ratio of the $^3H_4$-$^3F_4$ transition is defined as the ratio b/a, where a is the initial hole depth and b is a measure of the population in the shelving state.

1. Qiang, X. *et al.* Large-scale silicon quantum photonics implementing arbitrary two-qubit processing. *Nature Photonics* **12**, 534–539(2018).
2. Kimble, H. J. The quantum internet. *Nature* **453**, 1023–1030 (2008).
3. Aspuru-Guzik, A. & Walther, P. Photonic quantum simulators. *Nat. Phys.* **8**, 285–291 (2012).
4. He, Y. M. *et al.* Single quantum emitters in monolayer semiconductors. *Nat. Nanotechnol.* **10**, 497–502 (2015).
5. Chakraborty, C., Kinnischtzke, L., Goodfellow, K. M., Beams, R. & Vamivakas, A. N. Voltage-controlled quantum light from an atomically thin semiconductor. *Nat.*

Nanotechnol. **10**, 507–511 (2015).

6. Koperski, M. *et al.* Single photon emitters in exfoliated WSe2structures. *Nat. Nanotechnol.* **10**, 503–506 (2015).

7. Srivastava, A. *et al.* Optically active quantum dots in monolayer WSe2. *Nat. Nanotechnol.* **10**, 491–496 (2015).

8. Palacios-Berraquero, C. *et al.* Large-scale quantum-emitter arrays in atomically thin semiconductors. *Nat. Commun.* **8**, 1–6 (2017).

9. Kern, J. *et al.* Nanoscale Positioning of Single-Photon Emitters in Atomically Thin WSe2. *Adv. Mater.* 7101–7105 (2016) doi:10.1002/adma.201600560.

10. Kumar, S., Kaczmarczyk, A. & Gerardot, B. D. Strain-Induced Spatial and Spectral Isolation of Quantum Emitters in Mono- and Bilayer WSe2. *Nano Lett.* **15**, 7567–7573 (2015).

11. Monroe, C. Quantum information processing with atoms and photons [Review]. *Nature* **416**, 238–246 (2002).

12. Barnes, W. L., Dereux, A. & Ebbesen, T. W. Surface plamons subwavelength optics. *Nature* **424**, 824–830 (2003).

13. Schuller, J. A. *et al.* Plasmonics for extreme light concentration and manipulation. *Nat. Mater.* **9**, 193–204 (2010).

14. Huck, A. & Andersen, U. L. Coupling single emitters to quantum plasmonic circuits. *Nanophotonics* (2016) doi:10.1515/nanoph-2015-0153.

15. Pustovit, V. N. & Shahbazyan, T. V. Cooperative emission of light by an ensemble of

dipoles near a metal nanoparticle: The plasmonic Dicke effect. *Phys. Rev. Lett.* **102**, 1–4 (2009).

16. Hoang, T. B., Akselrod, G. M. & Mikkelsen, M. H. Ultrafast Room-Temperature Single Photon Emission from Quantum Dots Coupled to Plasmonic Nanocavities. *Nano Lett.* (2016) doi:10.1021/acs.nanolett.5b03724.

17. Matsuzaki, K. *et al.* Strong plasmonic enhancement of biexciton emission: Controlled coupling of a single quantum dot to a gold nanocone antenna. *Sci. Rep.* **7**, 1–11 (2017).

18. Chang, D. E., Sørensen, A. S., Hemmer, P. R. & Lukin, M. D. Quantum optics with surface plasmons. *Phys. Rev. Lett.* **97**, 1–4 (2006).

19. Fitzgerald, J. M., Narang, P., Craster, R. V., Maier, S. A. & Giannini, V. Quantum Plasmonics. *Proc. IEEE* **104**, 2307–2322 (2016).

20. Chang, D. E., Sørensen, A. S., Demler, E. A. & Lukin, M. D. A single-photon transistor using nanoscale surface plasmons. *Nat. Phys.* **3**, 807–812 (2007).

21. Nguyen, M. *et al.* Nanoassembly of quantum emitters in hexagonal boron nitride and gold nanospheres. *Nanoscale* **10**, (2018).

22. Tran, T. T. *et al.* Deterministic Coupling of Quantum Emitters in 2D Materials to Plasmonic Nanocavity Arrays. *Nano Lett.* **17**, 2634–2639 (2017).

23. Tripathi, L. N. *et al.* Spontaneous emission enhancement in strain-induced WSe2 monolayer based quantum light sources on metallic surfaces. *ACS Photonics* **5**, 5, 1919–1926 (2018).

24. E. M. Purcell, Phys. Rev. **69**, 681 (1946).

25. Sinclair, N., Oblak, D., Thiel, C. W., Cone, R. L. & Tittel, W. Properties of a Rare-Earth-Ion-Doped Waveguide at Sub-Kelvin Temperatures for Quantum Signal Processing. *Phys. Rev. Lett.* (2017) doi:10.1103/PhysRevLett.118.100504.

26. McPeak, K. M. *et al.* Plasmonic films can easily be better: Rules and recipes. *ACS Photonics* **2**, 326–333 (2015).

27. Huang, J. K., *et al.* Large-Area Synthesis of Highly Crystalline WSe_2 Monolayers and Device Applications *ACS Nano* **8**, 1, 923–930 (2014) doi:10.1021/nn405719x.

28. Castellanos-Gomez, A. *et al.* Deterministic transfer of two-dimensional materials by all-dry viscoelastic stamping. *2D Mater.* **1**, (2014).

29. Cai, T. *et al.* Coupling Emission from Single Localized Defects in Two-Dimensional Semiconductor to Surface Plasmon Polaritons. *Nano Lett.* **17**, 6564–6568 (2017).

30. Veronis, G. & Fan, S. Theoretical investigation of compact couplers between dielectric slab waveguides and two-dimensional metal-dielectric-metal plasmonic waveguides. *Opt. Express* **15**, 1211 (2007).

31. Yang, R., Wahsheh, R. A., Lu, Z. & Abushagur, M. A. G. Efficient light coupling between dielectric slot waveguide and plasmonic slot waveguide. *Opt. Lett.* **35**, 649 (2010).

32. Ajayai, O. *et al.* Approaching the Intrinsic Photoluminescence Linewidth in Transition Metal Dichalcogenide Monolayers. *2D Mater.* **4** 031011 (2017).

33. Thiel, C. W., Sun, Y., Macfarlane, R. M., Böttger, T. & Cone, R. L. Rare-earth-doped $LiNbO_3$ and $KTiOPO_4$ (KTP) for waveguide quantum memories. *J. Phys. B At. Mol. Opt. Phys.* (2012) doi:10.1088/0953-4075/45/12/124013.

34. Kunkel, N. & Goldner, P. Recent Advances in Rare Earth Doped Inorganic Crystalline Materials for Quantum Information Processing. *Zeitschrift für Anorg. und Allg. Chemie* **644**, 66–76 (2018).

35. Zhong, T. & Goldner, P. Review article Emerging rare-earth doped material platforms for quantum nanophotonics. *Nanophotonics* **8,** 11 (2019).

36. Thiel, C. W. & Böttger, T. Rare-Earth-Doped Materials with Application to Optical Signal Processing , Quantum Information Science , and Medical Imaging Technology. *SPIE OPTO* (2012) doi:10.1117/12.909154.

37. Kane, T. J. & Byer, R. L. Monolithic, unidirectional single-mode Nd:YAG ring laser. *Opt. Lett.* **10**, 65–67 (1985).

38. Equall, R. W., Sun, Y., Cone, R. L. & Macfarlane, R. M. Ultraslow optical dephasing in Eu^{3+}:Y_2SiO_5. *Phys. Rev. Lett.* **72**, 2179–2182 (1994).

39. Böttger, T., Thiel, C. W., Cone, R. L. & Sun, Y. Effects of magnetic field orientation on optical decoherence in Er^{3+}:Y_2SiO_5. *Phys. Rev. B* **79**, 115104 (2009).

40. Thiel, C. W., Böttger, T. & Cone, R. L. Rare-earth-doped materials for applications in quantum information storage and signal processing. *J. Lumin.* **131**, 353–361 (2011).

41. Li, Y. *et al.* Pulsed ultrasound-modulated optical tomography using spectral-hole burning as a narrowband spectral filter. *Appl. Phys. Lett.* **93**, 11111 (2008).

42. Zhong, M. *et al.* Optically addressable nuclear spins in a solid with a six-hour coherence time. *Nature* **517**, 177 (2015).

43. Heinze, G., Hubrich, C. & Halfmann, T. Stopped Light and Image Storage by

Electromagnetically Induced Transparency up to the Regime of One Minute. **033601**, 1–5 (2013).

44. Wesenberg, J. H., M\olmer, K., Rippe, L. & Kröll, S. Scalable designs for quantum computing with rare-earth-ion-doped crystals. *Phys. Rev. A* **75**, 12304 (2007).

45. Sangouard, N., Simon, C., de Riedmatten, H. & Gisin, N. Quantum repeaters based on atomic ensembles and linear optics. *Rev. Mod. Phys.* **83**, 33–80 (2011).

46. Chen, Y. Nanofabrication by electron beam lithography and its applications: A review. *Microelectron. Eng.* **135**, 57–72 (2015).

47. Zhong, T., Kindem, J. M., Rochman, J. & Faraon, A. Interfacing broadband photonic qubits to on-chip cavity-protected rare-earth ensembles. *Nature Communications* **8**, 14107 (2017) doi:10.1038/ncomms14107.

48. Zhong, T. *et al.* Optically addressing single rare-earth ions in a nanophotonic cavity. (2018) doi:arXiv:1803.07520v1.

49. Zhong, T. *et al.* Nanophotonic rare-earth quantum memory with optically controlled retrieval. *Science* **357**, 6358, 1392-1395 (2017) doi:10.1126/science.aan5959.

50. Saglamyurek, E. *et al.* Broadband waveguide quantum memory for entangled photons. *Nature* **469**, 512–515 (2011) doi:10.1038/nature09719.

51. Dibos, A. M., Raha, M., Phenicie, C. M. & Thompson, J. D. Atomic Source of Single Photons in the Telecom Band. *Phys. Rev. Lett.* **120,** 243601 (2018).

52. Jiang, X., Pak, D., Nandi, A., Xuan, Y. & Hosseini, M. Rare earth-implanted lithium niobate: Properties and on-chip integration. *Appl. Phys. Lett.* **115**, 71104 (2019).

53. Miyazono, E. *et al.* Coupling erbium dopants in yttrium orthosilicate to silicon photonic resonators and waveguides. *Optics Express* **7**, 2863–2871 (2017).

54. Ding, D. *et al.* Multidimensional Purcell effect in an ytterbium-doped ring resonator. *Nature Photonics* **10**, pages385–388, (2016).

55. Gong, Y. *et al.* Linewidth narrowing and Purcell enhancement in photonic crystal cavities on an Er-doped silicon nitride platform. *Opt. Express* **18**, 2601–2612 (2010).

56. Gong, Y. *et al.* Observation of Transparency of Erbium-doped Silicon nitride in photonic crystal nanobeam cavities. *Opt. Express* **18**, 13863–13873 (2010).

57. Becker, P., Brinkmann, R., Dinand, M., Sohler, W. & Suche, H. Er-diffused Ti:LiNbO3 waveguide laser of 1563 and 1576 nm emission wavelengths. *Appl. Phys. Lett.* **61**, 1257–1259 (1992).

58. Brüske, D., Suntsov, S., Rüter, C. E. & Kip, D. Efficient Nd:Ti:LiNbO3 ridge waveguide lasers emitting around 1085 nm. *Opt. Express* **27**, 8884–8889 (2019).

59. Sinclair, N. *et al.* Spectroscopic investigations of a Ti: Tm LiNbO3 waveguide for photon-echo quantum memory. in *Journal of Luminescence* (2010). doi:10.1016/j.jlumin.2009.12.022.

60. Staudt, M. U. *et al.* Interference of Multimode Photon Echoes Generated in Spatially Separated Solid-State Atomic Ensembles. *Phys. Rev. Lett.* **99**, 173602 (2007).

61. Zhang, M., Wang, C., Cheng, R., Shams-Ansari, A. & Loncar, M. Monolithic Ultrahigh-Q Lithium Niobate Microring Resonator. *Optica* **4**, 12, 1536-1537 (2017) doi:10.1364/OPTICA.4.001536.

62. Li, M., Liang, H., Luo, R., He, Y. & Lin, Q. High-Q 2D Lithium Niobate Photonic Crystal Slab Nanoresonators. *Laser and Photonics Reviews* **1800228**, 1–8 (2019).

63. Liang, H., Luo, R., He, Y., Jiang, H. & Lin, Q. High-quality lithium niobate photonic crystal nanocavities. *Optica* **4**, 10, 1251-1258 (2017) doi:10.1364/OPTICA.4.001251.

64. Sun, Y., Thiel, C. W. & Cone, R. L. Optical decoherence and energy level structure of 0.1%Tm 3+ :LiNbO 3. *Phys. Rev. B* **85**, 165106 (2012).

65. Magyar, A. *et al.* Synthesis of luminescent europium defects in diamond. *Nat. Commun.* **5**, 3523 (2014).

66. Scarafagio, M. *et al.* Ultrathin Eu- and Er-Doped Y2O3 Films with Optimized Optical Properties for Quantum Technologies. *J. Phys. Chem. C* **123**, 13354–13364 (2019).

67. Flinn, G. P. *et al.* Anomalous optical dephasing in crystalline Y2O3: Eu3+. *J. Lumin.* **58**, 374–379 (1994).

68. Chanelière, T. *et al.* Quantum Optical Memory Protocols in Atomic Ensembles. *Advances In Atomic, Molecular, and Optical Physics* 1–74 (2018).

69. Thiel, C. W., Sun, Y., Bttger, T., Babbitt, W. R. & Cone, R. L. Optical decoherence and persistent spectral hole burning in Tm^{3+}:$LiNbO_3$. in *Journal of Luminescence* (2010). doi:10.1016/j.jlumin.2009.12.019.

70. Krasnokutska, I., Chapman, R. J., Tambasco, J.-L. J. & Peruzzo, A. High coupling efficiency grating couplers on lithium niobate on insulator. *Opt. Express* **27**, 17681–17685 (2019).

71. He, L. *et al.* Low-loss fiber-to-chip interface for lithium niobate photonic integrated

circuits. *Opt. Lett.* **44**, 2314–2317 (2019).

72. Krasnokutska, I., Tambasco, J.-L. J. & Peruzzo, A. Nanostructuring of LNOI for efficient edge coupling. *Opt. Express* **27**, 16578–16585 (2019).

73. Wang, C. H., *et al.* Nanophotonic lithium niobate electro-optic modulators. *Optics Express* **26**, 1547–1555 (2018).

74. Nguyen, C. T. *et al.* Quantum Network Nodes Based on Diamond Qubits with an Efficient Nanophotonic Interface. *Phys. Rev. Lett.* **123**, 183602 (2019).

75. Sun, S., Kim, H., Luo, Z., Solomon, G. S. & Waks, E. A single-photon switch and transistor enabled by a solid-state quantum memory. *Science* **361**, 57 – 60 (2018).

76. Wilk, T., Webster, S. C., Kuhn, A. & Rempe, G. Single-Atom Single-Photon Quantum Interface. *Science* **317**, 488 – 490 (2007).

77. Afzelius, M., Simon, C., de Riedmatten, H. & Gisin, N. Multimode quantum memory based on atomic frequency combs. *Phys. Rev. A* **79**, 52329 (2009).

78. Dutta, S., Goldschmidt, E. A., Barik, S., Saha, U. & Waks, E. Integrated Photonic Platform for Rare-Earth Ions in Thin Film Lithium Niobate. *Nano Lett.* **20**, 741–747 (2020).

79. Kurnit, N. A., Abella, I. D. & Hartmann, S. R. Observation of a photon echo. *Phys. Rev. Lett.* **13**, 567–568 (1964).

80. Hahn, E. L. Spin echoes. *Phys. Rev.* **80**, 580–594 (1950).

81. Dutta, S., Goldschmidt, E., Barik, S., Saha, U. & Waks, E. Integrated Photonic Platform for Rare-Earth Ions in Thin Film Lithium Niobate. *Nano Lett.* **20**, 741–747.

82. Fossati, A. *et al.* A frequency-multiplexed coherent electro-optic memory in rare earth doped nanoparticles. *arXiv* (2020).